nature biotechnology

Article

https://doi.org/10.1038/s41587-026-03099-z

mRNA vaccine immunity is enhanced by hepatocyte detargeting and not dependent on dendritic cell expression

Received: 16 November 2024

Accepted: 20 March 2026

Published online: 29 April 2026

Check for updates

Adam Marks[1,2,3,6], Sophia Siu[1,2,3,6], Filippo Bianchini[1,2,3], Chunxi Wang[1,2,3], Ashwitha Lakshmi[1], Matthew Phelan[1], Andrew Zhu[4], Chang Moon[1,2,3], Judit Morla-Folch[1,5], Abraham J. P. Teunissen[1,5], Angelo Amabile[1,2,3], Alessia Baccarini[2,3], Miriam Merad[2,3,4], Joshua D. Brody[1,2,3,4], Yizhou Dong[1,2,3,4] & Brian D. Brown[1,2,3,4]

Proteins encoded by mRNA vaccines can be expressed by a diversity of transfected cell types but how cell-type-specific expression influences immunity is poorly understood. To investigate this, we incorporated synthetic microRNA target sites (miRT) into lipid nanoparticle (LNP)-delivered mRNA vaccines to silence mRNA expression specifically in professional antigen-presenting cells (pAPCs), hepatocytes or myocytes. We found that mRNA expression in pAPCs was dispensable for priming antigen-specific T cells, whereas mRNA expression in myocytes induced similar or stronger immune responses, including for SARS-CoV-2, suggesting that antigen cross-presentation or cross-dressing may be more impactful than direct mRNA expression in pAPCs. In contrast, mRNA expression in hepatocytes suppressed the antigen-specific T cell response, partly through PD1/PDL1. In mice bearing tumor-associated antigen (TAA)-expressing lymphoma cells, miRT-mediated hepatocyte-silenced TAA mRNA vaccine enhanced immune response and reduced tumor burden. Thus, non-pAPC expression shapes immunity to mRNA-encoded protein and inclusion of miRTs can boost or blunt mRNA-LNP immunogenicity.

mRNA is a new drug modality that enables transient expression of proteins, including Cas9 for gene editing, transcription factors for cell reprogramming, chimeric antigen receptors (CARs) for CAR T cells and viral or cancer antigens for vaccines[1–4]. The immune response to mRNA-encoded proteins is important for different applications of this drug modality. For vaccines, a strong immune response is the aim, whereas, for most other applications, such as gene editing, immunity should be avoided, particularly T cell immunity, which can eliminate cells expressing RNA-derived proteins such as Cas9.

With conventional vaccines that use inactivated pathogens or proteins, the antigen is presented to T cells by dendritic cells (DCs), which are unique in their ability to phagocytose exogenous antigen and process and present on major histocompatibility class I (MHC-I)[5]. In contrast, with mRNA vaccines, the encoded antigen can potentially be presented by whichever cells take up and express the RNA[6]. This is a key difference from traditional vaccines or protein and peptide drugs, as it broadens the cell types that can present the antigen to CD8 T cells beyond DCs. This is especially relevant to mRNA drugs because

[1]Icahn Genomics Institute, Icahn School of Medicine at Mount Sinai, New York, NY, USA. [2]Precision Immunology Institute, Icahn School of Medicine at Mount Sinai, New York, NY, USA. [3]Department of Immunology and Immunotherapy, Icahn School of Medicine at Mount Sinai, New York, NY, USA. [4]Tisch Cancer Institute, Icahn School of Medicine at Mount Sinai, New York, NY, USA. [5]Biomedical Engineering and Imaging Institute, Icahn School of Medicine at Mount Sinai, New York, NY, USA. [6]These authors contributed equally: Adam Marks, Sophia Siu. e-mail: brian.brown@mssm.edu

the RNA is delivered by lipid nanoparticles (LNPs), which transfect a broad range of cells, including hepatocytes, myocytes and professional antigen-presenting cells (pAPC), such as DCs[1].

While DCs were shown to be important for priming mRNA vaccine immunity[7], the influence of other transfected cell types, such as hepatocytes or myocytes, on the immune response to mRNA-encoded proteins is not known. Even with regard to DCs, the experimental data showed that DC depletion reduced RNA vaccine immunity[7]. However, it was not shown whether direct expression of the mRNA within DCs was necessary for immunity, as DC depletion would also prevent the presentation of exogenously derived antigens, similar to traditional vaccines. Thus, it is not known how the cellular expression pattern of mRNA vaccines and therapeutics influences immunity to mRNA-encoded proteins and this can affect their efficacy and safety.

We aimed to better understand how cell-intrinsic mRNA expression in pAPCs and non-pAPCs contributes to adaptive immunity to LNP-delivered mRNA-encoded proteins. To perform this in a tightly controlled manner, we used synthetic microRNA target sites (miRTs) to silence the expression of mRNA in specific cell types[8–10]. miRTs are sequences complementary to a specific miRNA, incorporated into the untranslated region (UTR) of mRNA[8,9,11–14]. If the mRNA enters a cell that does not express the cognate miRNA, the mRNA is translated; however, if the mRNA enters cells that express the miRNA, the miRNA will bind to the miRT and degrade the mRNA[11]. There are >1,000 miRNAs encoded in the mammalian genome, with many miRNAs having cell-specific expression patterns, such as miR-122 in hepatocytes[9,14], miR-142-3p in hematopoietic cells[15] and miR-133 and miR-206 in skeletal myocytes[16,17].

By incorporating specific miRTs into LNP-delivered mRNA, we can selectively silence mRNA expression in hepatocytes, pAPCs or skeletal muscle cells in vivo. We found that mRNA expression of antigen in pAPCs is not required for priming an antigen-specific immune response, whereas expression in muscle fibers boosts CD8 T cell expansion, suggesting that cross-presentation of mRNA-derived antigens may be more impactful than direct pAPC expression. mRNA expression in hepatocytes suppressed the quantity of payload-specific CD8 T cells and, by silencing mRNA in hepatocytes using an miRT for miR-122, intravenous (i.v.) mRNA-LNP vaccination led to a greater expansion of antigen-specific effector CD8 T cells and improved control of tumor burden. Silencing mRNA-LNP in hepatocytes also reduced hepatocyte killing by mRNA-boosted adoptively transferred antigen-specific T cells. These studies provide insight into how specific cellular expression patterns of mRNA-LNP influence the adaptive immune response to encoded proteins and show how incorporating miRT can control this response for RNA vaccines and therapeutics.

Results

mRNA silencing mediated by miR-142 and miR-122 is not affected by modified nucleosides

Several studies have shown that miRT can be used to regulate the expression of in vitro transcribed (IVT) mRNA[12–14,18,19] (Fig. 1a). We sought to better determine the level of control mediated by the incorporation of miRT into IVT mRNA. We first tested how the number of miRNA-binding sites affects mRNA expression. We cloned one or four perfectly complementary miRTs for the hepatocyte-specific miRNA, miR-122 (122T), into the UTR of a GFP-encoding mRNA. After IVT, we encapsulated the mRNA into an LNP and transfected AML12 hepatocytes, which express miR-122. With a single 122T, there was a 50% reduction in GFP$^+$ AML12 cells compared to wild-type mRNA (RNA.WT) (Fig. 1b). With four 122Ts in the mRNA's UTR (RNA.122T), there was a near-complete silencing of mRNA expression in the hepatocytes, as indicated by a >95% reduction in GFP$^+$ cells, demonstrating miRT copy-number-dependent silencing.

Modified bases, such as pseudouridine (ΨU), 5-methylcytosine (m5C) or N^1-methylpseudouridine (N1m), are commonly used to improve stability and reduce innate immunogenicity of IVT mRNA[20,21]. As there are conflicting reports on how modified bases influence miRNA-mediated silencing[12,22], we tested this here. We generated GFP-encoding RNA.WT or RNA.122T, as well as an RNA with miRT for the hematopoietic-specific miRNA, miR-142 (RNA.142T), with each of the modified bases. The mRNA was encapsulated in LNPs and different cells transfected. miRT incorporation did not affect mRNA expression in non-miRNA-expressing cells (293T) and this was independent of RNA modification (Fig. 1c). Inclusion of miRT in a Cas9-encoding mRNA also did not impair the ability to transfect and edit a gene (Extended Data Fig. 1a). With all modified bases, there was robust silencing of the RNA.miRT in cell types expressing the cognate miRNA (Fig. 1c). Even with N1m, which led to the highest expression of mRNA, inclusion of the miRT led to robust cell-type-specific silencing. These results demonstrate that endogenous miRNA can mediate silencing of modified RNA as effectively as unmodified RNA.

miRTs enable selective mRNA silencing in fibroblasts, B cells and activated macrophages

We looked to expand the cell types that can be detargeted using miRTs. We examined a database of miRNA expression profiles[23] and identified miR-214 as highly expressed in fibroblasts, miR-190b as high in B cells and miR-155 as upregulated in activated macrophages and DC. We cloned miRTs for each miRNA into GFP-encoding mRNA (substituted with N1m) and encapsulated in an LNP with SM-102-ionizable lipid[24]. We confirmed equivalent mRNA concentration, encapsulation efficiency and functional capacity of all mRNA-LNPs through physical measures, Ribogreen assays and transfection of 293T cells, which do not express any of the miRNAs (Supplementary Fig. 1a–e).

Transfection of RAW264.7 macrophages with RNA.214T and RNA.190T resulted in similar GFP levels (Fig. 1d), consistent with the lack of miR-214 and miR-190b in macrophages[23]. Transfection of NIH3T3 fibroblasts with RNA.142T and RNA.190T resulted in >95% GFP$^+$ cells, whereas, with RNA.214T, GFP expression in fibroblasts was abolished or reduced to near-background levels. RNA.190T expression was specifically suppressed in BCL1 B cells, with a tenfold reduction in the number of GFP$^+$ B cells compared to RNA.214T.

miRNAs are highly conserved between mouse and human, with the majority of high-abundance miRNAs being sequence identical[25]. To test silencing of the same mRNA formulation, we transfected human hepatocytes (HuH7) with GFP RNA.WT and RNA.122T. Similar to mouse

Fig. 1 | miRNA silences native and modified mRNA in different cell lineages and states. a, Schematic of miRNA-based regulation strategy for IVT mRNA expression. **b**, Flow cytometry analysis of GFP expression in AML12 hepatocytic cells 24 h after transfection with GFP-encoding RNA.WT or RNA.122T (100 ng ml^{-1} per well). Mean expression values were normalized to the untransfected (UT) control and data are presented as the mean ± s.e.m. ($n = 3$ biological replicates). **c**, Bar graphs showing the relative GFP mean fluorescence intensity (MFI) from flow cytometry analysis of HEK293T, RAW264.7 and AML12 18 h after transfection with native or modified mRNA constructs ($n = 3$) (100 ng ml^{-1} per well). The detection threshold (dotted line) was defined by the MFI of respective UT cells. Data are shown as the mean ± s.e.m. ($n = 3$). **d**, Flow cytometry analysis of HEK293T, RAW264.7, 3T3/NIH and BCL1 cells transfected with GFP RNA-LNP with the indicated miRT (100 ng ml^{-1} per well). The mean GFP expression (%GFP$^+$) is stratified by cell type and miRT-encoded sequences. Statistical comparisons were made using unpaired Student's *t*-tests between cells transfected with RNA.WT and RNA.miRT. Bars represent the mean ± s.e.m. ($n = 3$). **e**, Flow cytometry analysis of primary murine bone-marrow-derived macrophages (BMDMs; F480$^+$/CD11b$^+$), stimulated with LPS for 24 h. Cells were cotransfected with GFP RNA.155T and mCherry RNA.WT encapsulated in LNPs (50 ng ml^{-1} per construct per well). Top: dot plots are representative of $n = 3$ biological replicates. Bottom: bar graph showing mean GFP expression normalized to mCherry expression (transfection control). Data are shown as the mean ± s.e.m. ($n = 3$). Significance was determined using an unpaired two-sided Student's *t*-test, unless otherwise specified. Panels **a**, **b** and **d** created in BioRender; Baccarini, A. https://biorender.com/1x1s0aw (2026).

https://doi.org/10.1038/s41587-026-03099-z

hepatocytes, there was complete silencing of RNA.122T. Silencing was dependent on miR-122, as transfection of the hepatocytes with a miR-122 antagomiR, led to a dose-dependent increase in GFP in cells transfected with RNA.122T (Extended Data Fig. 1b).

To assess the potential to silence mRNA specifically in activated pAPCs[26], we generated RNA with miRT for miR-155 (ref. 27). We generated bone-marrow-derived macrophages and kept them immature or activated with LPS and then cotransfected with GFP RNA.155T and

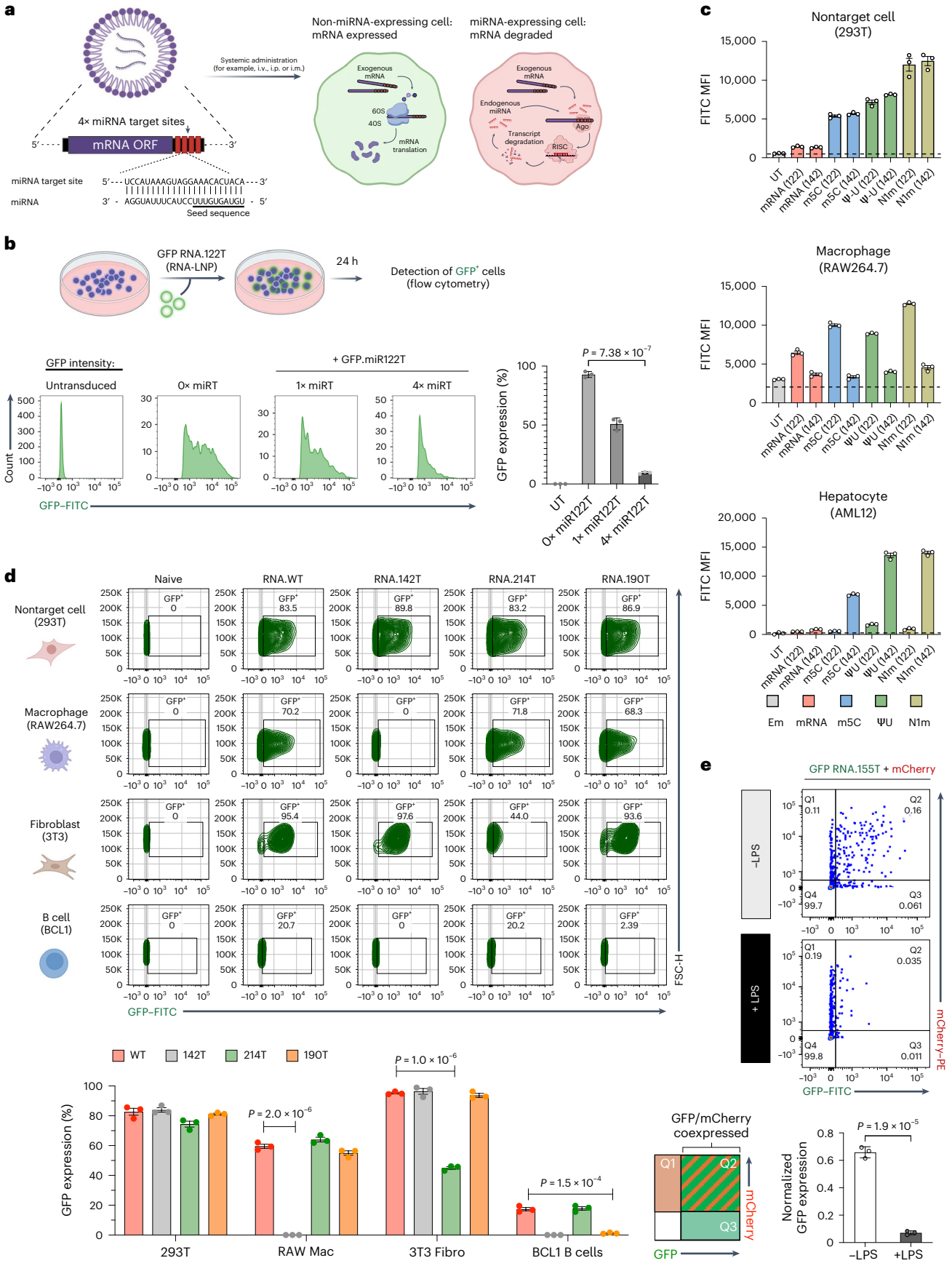

mCherry RNA.WT. Flow cytometry indicated that ~0.25% of cells were mCherry$^+$ in untreated and LPS-treated macrophages, whereas 0.2% of immature macrophages were GFP$^+$ and <0.0035% of LPS-activated macrophages were GFP$^+$ (Fig. 1e). This represents a >4-fold reduction in mRNA expression specifically in activated macrophages by including 155Ts.

These results show how miRTs can be rationally selected by miRNA expression profiles to control mRNA expression in a cell-specific manner.

122Ts silence mRNA specifically in hepatocytes

The i.v. injection of most RNA-LNP formulations results in significant transfection and expression in not only hepatocytes[1,4] but also other cell types, including macrophages, monocytes and DCs (Extended Data Fig. 2a–f). Intramuscular (i.m.) injection also results in the transfection of different cell types, including myocytes in the muscle[28,29] and pAPCs in the spleen and draining lymph nodes (dLNs); however, even with i.m. injection, cells in the liver are transfected (Extended Data Fig. 2a–g). This is a result of the high propensity of LNPs to be taken up by hepatocytes[4,30]. While this is beneficial for liver-targeted therapies, hepatotropism can be detrimental when the RNA cargo is toxic to hepatocytes[1]. For this reason, several groups developing extrahepatic therapies have included 122Ts in their RNA[14,19]. However, prior studies characterized the suppressive activity of 122T on IVT RNA at a bulk organ level using luciferase[14].

To assess the level of control mediated by the inclusion of 122T at cellular resolution, we generated a Cre RNA.WT or RNA.122T, encapsulated it in LNP and i.v. injected 20 µg into Ai14 mice, which carry a tdTomato expression cassette flanked by LoxP sites (Fig. 2a). Gross organ measurement indicated that there was a major reduction in tdTomato expression from RNA.122T compared to RNA.WT in the liver but no differences in the spleen (Fig. 2b). With RNA.122T, there was a major reduction in the number of tdTomato$^+$ hepatocytes (Fig. 2c); however, interstitial cells of the liver, which include Kupffer cells and endothelial cells, were still tdTomato$^+$. In the spleen, RNA.WT and RNA.122T resulted in similar numbers of tdTomato$^+$ splenocytes (Fig. 2d), indicating that 122T did not affect Cre mRNA expression in nonhepatic cells.

We repeated our analysis with mRNA encoding GFP. We encapsulated GFP RNA.WT or RNA.122T in the same LNP formulation, i.v. injected mice and analyzed tissues after 24 h. Imaging of the liver revealed a ~150-fold reduction in the number of GFP$^+$ hepatocytes mediated by the inclusion of 122T in the mRNA, with an average of ~800 GFP$^+$ hepatocytes per mm^2 in mice injected with RNA.WT and <20 GFP$^+$ hepatocytes per mm^2 with RNA.122T (Fig. 2e). There was no loss of hepatocyte silencing of RNA.122T even after three i.v. injections, demonstrating the robustness of miR-122 control of mRNA treatment (Extended Data Fig. 3a–c). Liver macrophages and endothelial cells were GFP$^+$ in RNA.122T-injected mice, indicating that silencing was specific to hepatocytes (Fig. 2f,g). Injection of both RNA.WT and RNA.122T induced some elevation in inflammatory proteins in the blood, measured at 24 h, consistent with the adjuvant properties of RNA-LNP[31]. This included increased chemokines CXCL9, CCL2, CCL3 and CCL5 and cytokines IL-10, TNF and CSF2 (Extended Data Fig. 3d). However, there were no differences between RNA.WT and RNA.122T, indicating that miRT inclusion altered only mRNA expression and not the innate response to the RNA-LNP (Extended Data Fig. 3e).

These results confirm that incorporation of 122T eliminates hepatocyte expression without affecting nonhepatocyte expression of LNP-delivered mRNA.

142Ts mediate robust mRNA silencing across immune cell types

To determine how effectively inclusion of 142T would silence mRNA in primary pAPCs, we removed the spleen from mice and then dissociated and transfected 5×10^5 splenocytes with 1 µg of GFP-encoding RNA. WT or RNA.142T (Fig. 2h) that were confirmed to be concentration matched (Supplementary Fig. 1e). After 18 h, we analyzed the cells by flow cytometry. With GFP RNA.WT, ~8% of macrophages, 16% of DCs and 3% of monocytes were GFP$^+$, whereas, with GFP RNA.142T, there was no GFP detected in any pAPCs (similar to Cre RNA, a negative control) (Fig. 2h). T cells, B cells and neutrophils were also GFP$^-$ with GFP RNA.142T.

We assessed whether incorporation of the miRT alters the innate response to RNA-LNP. We transfected bone-marrow-derived DCs with GFP RNA.WT or RNA.142T and found no differences in inflammatory protein production, as measured by a 96-protein Olink panel or by reverse transcription (RT)–qPCR (Extended Data Fig. 4a,b). This further indicates that miRT inclusion does not alter the innate-activating properties of RNA-LNP.

Next, we i.v. injected mice with 20 µg of LNP-encapsulated GFP RNA.WT or RNA.142T (Fig. 2i). Once again, equivalent functional concentrations were first verified on 293T cells (Supplementary Fig. 2). We also injected an LNP containing Cre RNA.WT (no GFP) as a control. After 18 h, we analyzed GFP expression in the spleen by flow cytometry (Supplementary Fig. 3). Macrophages, DCs, B cells and T cells were all GFP$^-$ in RNA.142T-injected mice, whereas they were GFP$^+$ in mice injected with RNA.WT (Fig. 2i). The only hematopoietic cell type in which there were any GFP$^+$ cells detected with RNA.142T were monocytes but the number of GFP$^+$ cells was >50% reduced from RNA. WT and only marginally higher than the negative control. When we isolated monocytes from the spleen and immediately transfected them with 1 µg of RNA-LNP, ~15% of monocytes were GFP$^+$ with RNA.WT but there were no GFP$^+$ cells with RNA.142T (Extended Data Fig. 4c), confirming the results of the total spleen explant. As monocytes can phagocytose antigens and we did not detect GFP in monocytes ex vivo (with a relatively higher direct dose), the modest GFP signal in

Fig. 2 | 122T and 142T mediate specific and robust mRNA-LNP silencing in hepatocytes and hematopoietic cells in vivo. a, Schematic of the experimental setup for **b**–**g**. TVI, tail-vein injection. **b**, Whole-organ fluorescence imaging and quantification of MFI in liver and spleen following i.v. injection of Ai14 mice ($n = 3$ mice per group, repeated 3 independent times) with 20 µg of Cre RNA. WT or RNA.122T encapsulated in LNPs. Data are presented as the mean ± s.d. **c**, Immunofluorescence imaging of frozen unfixed liver and spleen sections from **b**. Representative image showing staining for tdTomato (red) and DAPI counterstaining for nuclei (blue). Scale bars, 100 µm. **d**, Quantification of tdTomato$^+$ immune cells (CD45$^+$) from spleen of mice from **b**. Representative flow plots (top) and a graph with the mean ± s.d. (bottom) are shown. **e**, Liver sections stained for GFP expression using IHC ($n = 3$ mice group, repeated 3 independent times) 24 h after i.v. injection with 20 µg of RNA.WT or RNA.122T. GFP$^+$ cells are indicated by yellow arrowheads. Right: bar graph showing the mean quantification of GFP$^+$ hepatocytes per unit area. Scale bars, 50 µm. Data are presented as the mean ± s.d. **f**, Representative image of liver from animal injected with GFP RNA.122T from **e** stained for GFP (green), CD31 (red) and F4/80 (magenta). Scale bars, 50 µm. **g**, Highlighted regions from **f** indicating specific GFP$^+$ populations, identified by counterstaining as GFP$^+$ endothelial cells (CD31$^+$, yellow arrowheads) and liver macrophages (F4/80$^+$, white arrowheads). Scale bars, 40 µm. **h**, Flow cytometry analysis of immune cells from spleen explants cultured for 18 h with GFP RNA.WT or GFP RNA.142T encapsulated in LNPs. Left: representative dot plots shown for hematopoietic cells (CD45$^+$) and DCs (Cd11c$^+$ MHC-II$^+$). Right: bar graph showing the mean proportion of GFP-expressing cells for each immune cell type ($n = 3$ biological replicates). Data are presented as the mean ± s.e.m. **i**, Flow cytometry analysis of GFP expression in spleens of mice 24 h after i.v. injection with 20 µg of GFP RNA.WT or GFP RNA.142T in LNPs. Left: representative dot plots shown for hematopoietic cells (CD45$^+$) and B cells (B220$^+$CD19$^+$). Right: bar graph showing the mean proportion of GFP-expressing cells for each immune cell type ($n = 3$ biological replicates). Data are presented as the mean ± s.e.m. Significance was determined using an unpaired two-tailed Student's t-test. Panels **a**, **h** and **i** created in BioRender; Baccarini, A. https://biorender.com/1x1s0aw (2026).

https://doi.org/10.1038/s41587-026-03099-z

RNA.142T-treated mice likely stems from antigen uptake from non-hematopoietic cells expressing antigens, as discussed below. These data indicate that 142T robustly silences RNA expression in pAPCs and other hematopoietic cells.

mRNA expression in DCs is not required for priming antigen-specific immune response

DCs are considered essential for RNA vaccine-induced immunity, evidenced by experiments in DC-depleted mice[7]. However, it is not

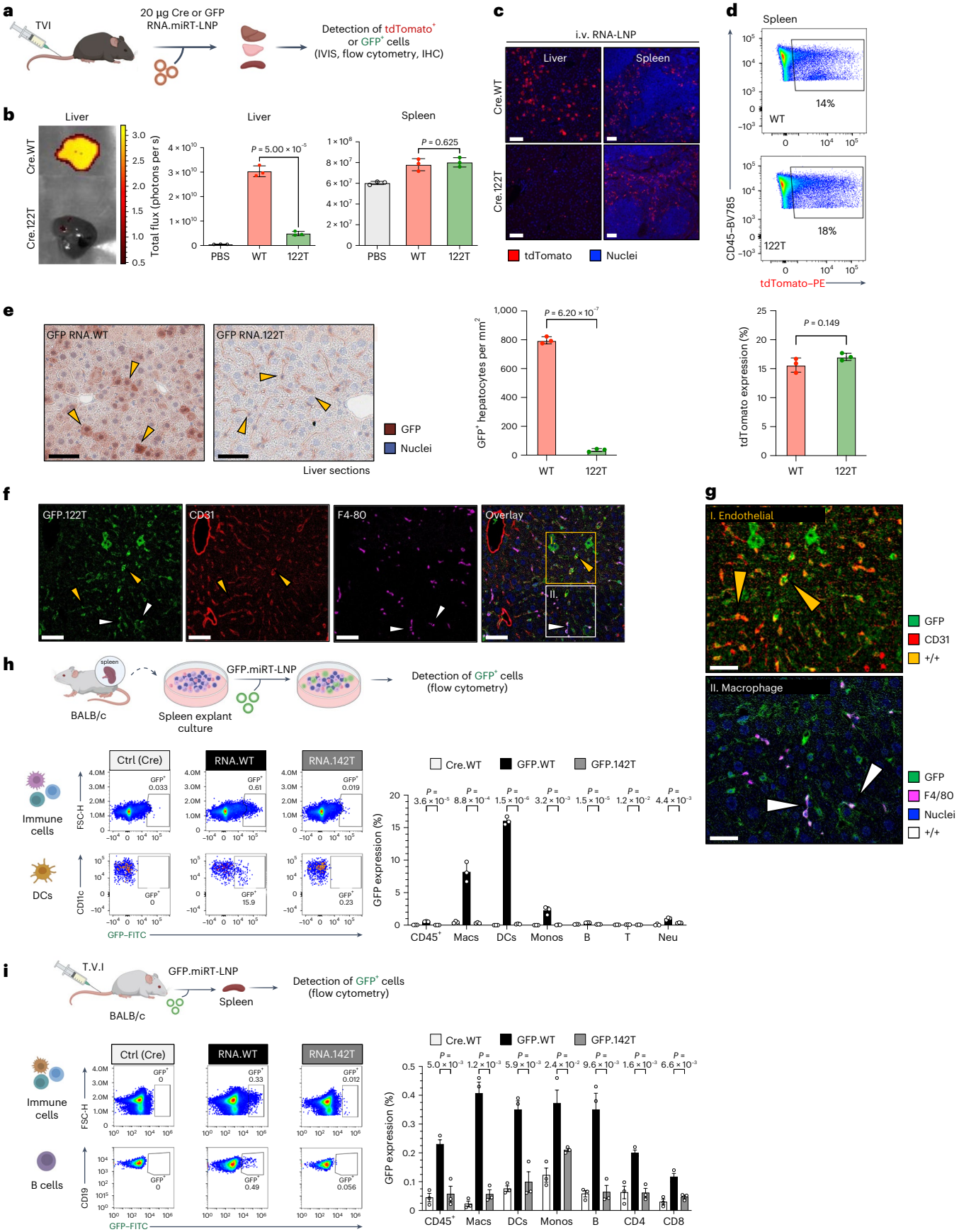

https://doi.org/10.1038/s41587-026-03099-z

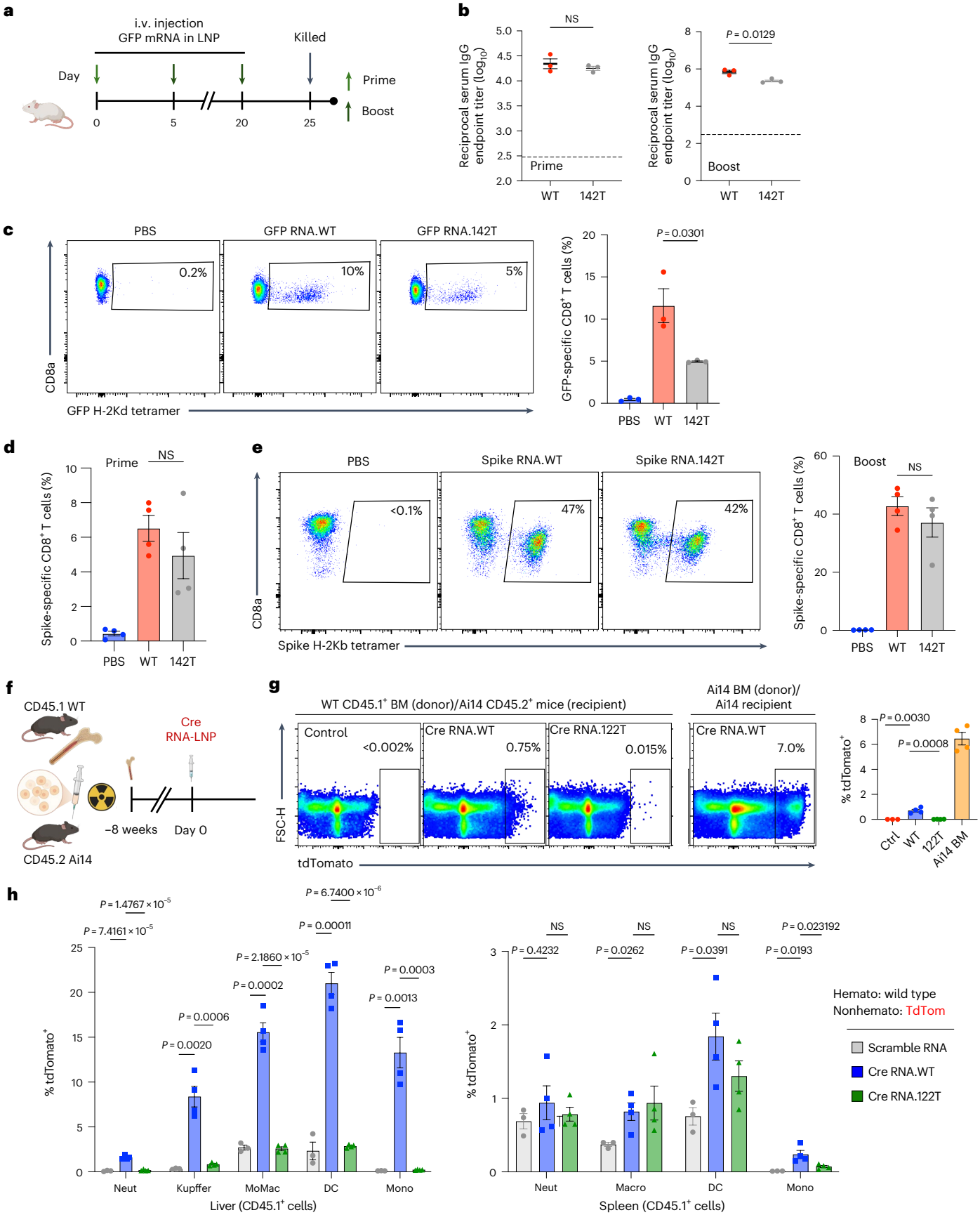

yet established whether intrinsic RNA expression within DCs is essential, as DCs also prime immunity through antigen uptake, which is how many traditional vaccines work[32,33]. Our biodistribution studies demonstrated that 142T completely silenced mRNA expression in DCs in vivo. Thus, using miRT enables us to investigate the contribution of intrinsic DC expression without modifying the LNP or depleting DCs, which can alter the innate response[7,33,34] and complicate interpretation of results.

Fig. 3 | Assessment of CD8$^+$ T cell response to hematopoietically silenced RNA-LNP and nonhematopoietic antigen transfer to pAPCs. a, Schematic indicating vaccine schedule for **b** and **c**. BALB/c mice ($n = 3$ per group, repeated 2 independent times) were injected i.v. with 20 µg of GFP RNA.WT or RNA.142T on days 0, 5 and 20. **b**, Anti-GFP IgG antibody titers in sera were assessed on days 10 (prime; 5 days after prime) and 25 (boost; 5 days after second boost). The limit of detection is indicated by a dotted line. Each dot is an individual animal. **c**, Frequency of GFP-specific CD8$^+$ T cells in the spleen was quantified by flow cytometry. Representative dot plots (left) and a graph with the mean ± s.e.m. (right) are shown, where dots denote individual mice. **d**, C57BL/6 mice ($n = 4$ per group) were injected i.m. with 5 µg of Spike RNA.WT or RNA.142T on days 0 and 21. The graph shows the frequency of Spike-specific CD8$^+$ T cells in the blood at 7 days after the priming dose. Quantification was performed by CD8 and tetramer staining and quantified by flow cytometry. **e**, Frequency of Spike-specific CD8$^+$ T cells in the spleen of mice from **d** at 5 days after boost. Representative dot plots (left) and a graph of the mean ± s.e.m. (right) are shown, where each dot denotes an individual mouse. **f**, Schematic showing experimental design for **g** and **h**. Lethally irradiated CD45.2$^+$ Ai14 mice ($n = 4$ mice per group) were reconstituted with CD45.1$^+$ WT bone marrow. After 8 weeks, mice were i.v. injected with irrelevant RNA (Ctrl) or Cre RNA.WT or RNA.122T. As a positive control, recipient Ai14 mice were reconstituted with Ai14 bone marrow before Cre RNA.WT injection. **g**, tdTomato expression in liver CD45.1$^+$ cells for WT bone marrow donor groups and CD45.2$^+$ cells for Ai14 bone marrow donor group 3 days after injection was analyzed by flow cytometry. Representative flow cytometry plots (left) and a graph of the mean ± s.e.m. (right) are shown. **h**, tdTomato expression in liver (left) and spleen (right) CD45.1$^+$ myeloid subsets were analyzed by flow cytometry. Error bars indicate the mean ± s.e.m. NS, not significant. Significance was determined using an unpaired two-tailed Student's *t*-test. Panels **a** and **f** created in BioRender; Baccarini, A. https://biorender.com/1x1s0aw (2026).

We primed and boosted mice with GFP-encoding RNA.WT or RNA.142T encapsulated in LNPs (Fig. 3a). Measurement of anti-GFP antibodies found comparable titers between RNA.WT and RNA.142T (Fig. 3b). On day 25, we quantified GFP-specific CD8$^+$ T cells in the spleen using a tetramer specific to the immunodominant epitope of GFP ($GFP_{200–208}$) loaded onto MHC-I. As with the antibodies, mRNA expression in DCs or other pAPCs was not required for the induction of GFP-specific CD8$^+$ T cells, although there was a decrease in quantity, with 10% of CD8$^+$ T cells being GFP specific in RNA.WT-treated animals and 5% being GFP specific in RNA.142T-treated animals (Fig. 3c).

To assess the importance of intrinsic pAPC expression on the response to a real-world antigen, we generated RNA.WT and RNA.142T encoding SARS-CoV-2 Spike and performed prime and boost through i.m. injection. Notably, there was no difference in Spike-specific CD8$^+$ T cells between the two formulations, despite no direct expression of RNA.142T in pAPCs (Fig. 3d,e). Similarly, there was no difference in ovalbumin (OVA)-specific CD8 T cells between OVA-encoding RNA.WT or RNA.142T vaccination (Extended Data Fig. 5a).

These results were unexpected as pAPCs are required for priming antigen-specific T cells[26] and the ability of RNA-LNPs to transfect DCs and intrinsically produce antigen for MHC-I presentation is considered an important feature in RNA-LNP efficacy[35]. We hypothesized that, although DCs were not directly expressing the mRNA, they were acquiring antigens from RNA-LNP-transfected cells. To test this, we transplanted WT CD45.1$^+$ bone marrow into lethally irradiated CD45.2$^+$ Ai14 mice (Fig. 3f). After reconstitution, the mice had WT hematopoietic cells (no tdTomato gene) and Ai14 nonhematopoietic cells. We then injected them with Cre-encoding RNA-LNPs. Despite not encoding a tdTomato gene, ~10–20% of CD45.1$^+$ macrophages and DCs in the liver were tdTomato$^+$, indicating that they acquired exogenous antigen from transfected nonhematopoietic cells (Fig. 3g,h). In the liver, the source of tdTomato was hepatocytes, as injection of Cre RNA.122T led to a loss of tdTomato$^+$ hepatic pAPCs. In the spleen, 1–2% of CD45.1$^+$ macrophages and DCs were tdTomato$^+$, even with injection of RNA.122T (Fig. 3h and Extended Data Fig. 5b,c), indicating that they obtained tdTomato from a nonhepatocyte, nonhematopoietic source.

To assess whether exogenous uptake of antigen might occur following i.m injection, we injected Ai14 mice with Cre-encoding RNA.WT or RNA.142T. With RNA.142T, there was a >20-fold reduction in tdTomato within CD45$^+$ immune cells in the dLN compared to RNA.WT. Importantly, in the few residual tdTomato$^+$ cells of RNA.142T-injected mice, there was a complete loss of tdTomato^{hi} cells, indicating exogenous tdTomato uptake rather than constitutive tdTomato expression from the ROSA26/CAG-promoter following Cre-mediated recombination (Extended Data Fig. 5d–f). To assess whether transfected muscle cells might be a source of antigens, we transfected C2C12 myocytes with GFP RNA.WT or RNA.142T. After washing, we cocultured them with RAW macrophages. Within 24 h, ~12% of macrophages became GFP$^+$. This occurred even with myocytes transfected with RNA.142T, which is silenced in macrophages, indicating that protein was transferred. This demonstrates, at least in vitro, that transfected muscle cells can release antigens that are taken up by pAPCs (Extended Data Fig. 5g,h).

These experiments reveal that in vivo delivered mRNA does not need to be directly expressed in DCs or other pAPCs to induce immunity to the payload and suggest that cross-delivery of antigen from RNA-LNP-transfected non-pAPCs can provide a compensatory source of antigens for CD8 T cell activation. This challenges a key assumption of mRNA vaccine effectiveness and is relevant for the design of mRNA therapeutics in which immunity is unwanted.

Fig. 4 | RNA-LNP expression in hepatocytes dampens antigen-specific CD8$^+$ T cell response. a, Schematic of vaccine schedule for **b**. BALB/c mice were injected i.v. with 20 µg of GFP RNA.WT or RNA.122T in LNP on days 0, 5 and 20 ($n = 3$ per group, repeated 2 independent times). **b**, Frequency of GFP-specific CD8$^+$ T cells in the spleen quantified by flow cytometry. Representative dot plots (left) and a graph with the mean ± s.e.m. (right) are shown. **c**, Schematic of the experimental setup for **d**–**k**. BALB/c mice were subcutaneously implanted with GFP-expressing A20 lymphoma cells. Then, 20 µg of GFP RNA.WT or RNA.122T or mCherry RNA (Ctrl) LNP was i.v. injected on days 4, 7, 11 and 15 ($n = 5$ mice per group, repeated 2 independent times). **d**, Tumor growth curves (mean ± s.e.m. of $n = 5$ mice per cohort). **e**, Representative images of tumors collected at 20-day endpoint. **f**, Quantification of GFP-specific CD8$^+$ T cells ($GFP_{200–208}$ H-2K^d tetramer$^+$) per gram of tumor. Quantification was performed by flow cytometry. Note that T cells are from tumors of different starting sizes depending on treatment. Data are presented as the mean ± s.e.m. **g**, Frequency of GFP-specific CD8$^+$ T cells in the spleen of tumor-bearing mice vaccinated as indicated in **c**. Data are presented as the mean ± s.e.m. **h**, Quantification of TIM3 and PD1 expression on tumor-infiltrating GFP-specific CD8$^+$ T cells by flow cytometry. Left: representative dot plots. Right: graphs showing the frequency of intratumoral TIM3$^+$PD1$^+$ GFP-specific CD8$^+$ T cells and the MFI of TIM3 and PD1 on cells. Data are presented as the mean ± s.e.m. **i**, MFI of TIM3 on GFP-specific CD8$^+$ T cells in the spleen of tumor-bearing mice. Data are presented as the mean ± s.e.m. **j**, Quantification of tumor-infiltrating CD44$^+$CD8$^+$T cells from mice. Data are presented as the mean ± s.e.m. **k**, Quantification of IFNγ and granzyme B production by intratumoral CD8$^+$ T cell upon in vitro restimulation with $GFP_{200–208}$ peptide-pulsed APCs. Data are presented as the mean ± s.e.m. **l**, Left: frequency of GFP-specific CD8$^+$ T cells in the spleen of BALB/c mice prime and boosted with GFP RNA.WT or RNA.122T and receiving anti-PD1 or IgG isotype control. Right: fold change in percentage of GFP-specific CD8$^+$ T cells between groups treated with IgG isotype and anti-PD1. Graphs show the mean ± s.e.m. ($n = 5$ mice per group). **m**, Quantification of granzyme B$^+$ splenic CD8$^+$ T cells upon in vitro restimulation with $GFP_{200–208}$ peptide-pulsed APCs (from $n = 5$ mice per group). Data are presented as the mean ± s.e.m. Significance was determined using an unpaired two-tailed Student's *t*-test. Panels **a** and **c** created in BioRender; Baccarini, A. https://biorender.com/1x1s0aw (2026).

https://doi.org/10.1038/s41587-026-03099-z

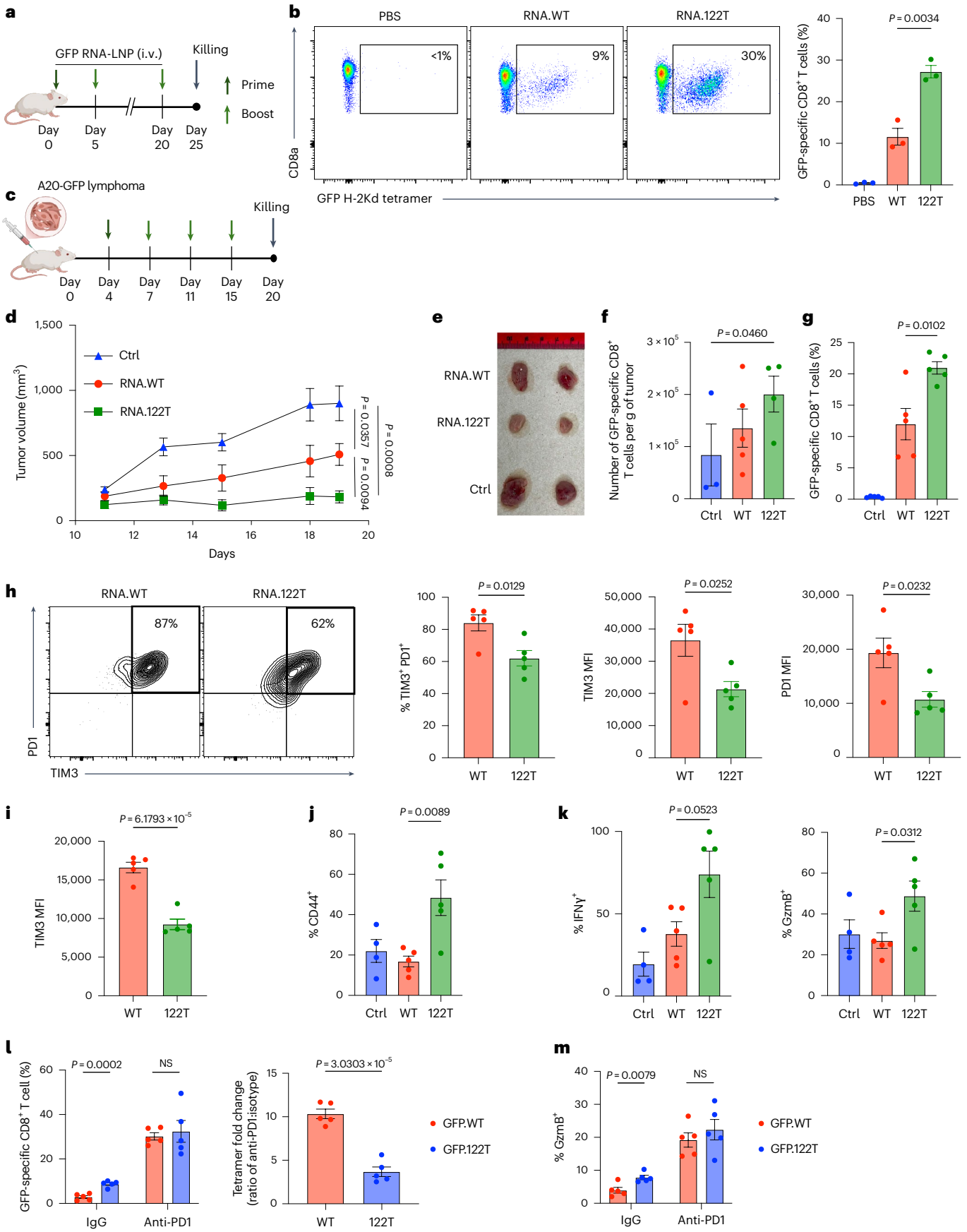

https://doi.org/10.1038/s41587-026-03099-z

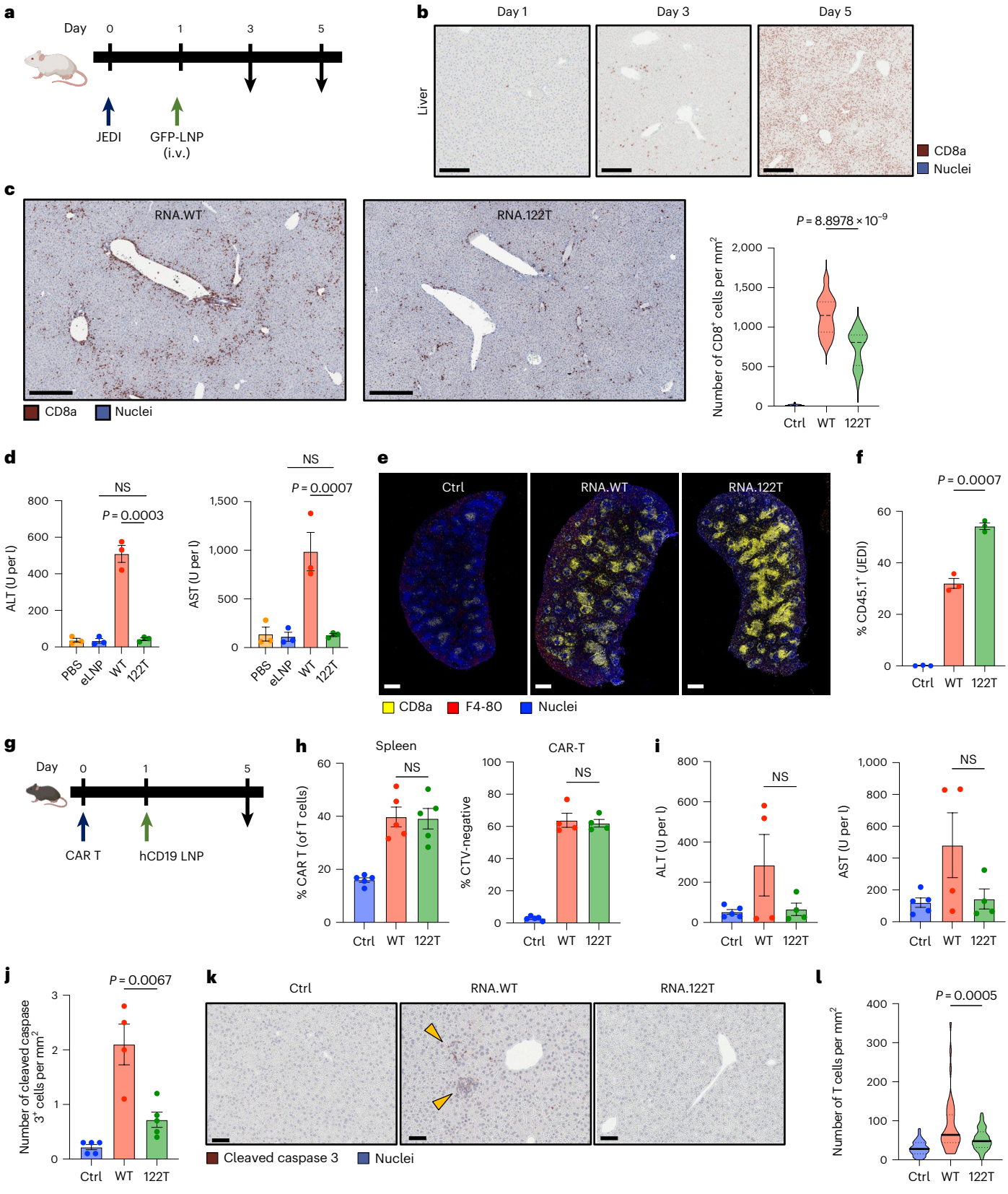

mRNA expression in hepatocytes reduces the magnitude of antigen-specific T cells and dampens cancer vaccine effectiveness

Hepatocytes are efficiently transfected by RNA-LNPs in vivo; thus, we sought to determine how they might contribute to RNA-encoded protein immunity. We i.v. injected mice in a three-dose vaccination schedule with GFP-encoding RNA.122T (Fig. 4a). There was no increase in anti-GFP antibody titer (Extended Data Fig. 6). However, there was a significant increase in the T cell response, with RNA.122T leading to ~28% of total CD8$^+$ T cells being GFP specific compared to just 10% GFP-specific T cells with RNA.WT (Fig. 4b). This is ~3-fold increase in antigen-specific T cells, using the same RNA-LNP dose

https://doi.org/10.1038/s41587-026-03099-z

Fig. 5 | Hepatocyte silencing of mRNA reduces liver T cell infiltration and toxicity. a, Schematic of the experimental set for **b**–**f**. CD45.2$^+$ BALB/c mice ($n = 3$ mice, repeated 3 independent times) received adoptive transfer of CD45.1$^+$ Jedi CD8$^+$ T cells. The next day, mice were i.v. injected with 20 µg of GFP RNA.WT, RNA.122T or RNA.142T LNP or empty LNP (Ctrl). Empty LNPs were formulated with no mRNA. **b**, Representative images of liver sections from mice injected with GFP RNA.WT, stained for CD8a to show CD8$^+$ T cell infiltration on days 1, 3 and 5 after injection. Scale bars, 50 µm. **c**, Quantification of CD8$^+$ T cell infiltration in the liver of mice injected 5 days earlier with empty LNP (Ctrl or eLNP) or GFP RNA.WT or GFP RNA.122T encapsulated in LNPs. Left: representative images shown for RNA.WT and RNA.122T. Right: graph showing the quantification of CD8a$^+$ cells per mm^2 ($n = 10$ regions of interest (ROIs) from $n = 3$ mice per group, repeated at least 3 independent times). The central line indicates the median and box edges show the interquartile range. Significance was determined using an unpaired two-tailed Student's *t*-test. Scale bars, 100 µm. **d**, Serum ALT and AST levels on day 5 after injection from mice in **a**. Significance was determined using a one-way analysis of variance followed by Tukey's multiple-comparison test. **e**, Imaging of T cells in the spleens of vaccinated mice. Representative images stained for CD8a (yellow), F4/80 (red) and nuclei (blue) are shown. Scale bars, 800 µm. **f**, Frequency of GFP-specific Jedi T cells (CD45.1$^+$) within CD8$^+$ T cells in spleens of mice 5 days after injection measured by flow cytometry. Significance was determined using an unpaired two-tailed Student's *t*-test. **g**, Schematic of the experimental setup for **h**–**l**. A total of 5×10^6 hCD19 CAR T cells (generated from C57BL/6 CD45.1$^+$ T cells) were transferred into lymphodepleted CD45.2$^+$ C57BL/6 mice ($n = 5$ mice per group) and, on the following day, mice were i.v. injected with 20 µg of hCD19-encoding RNA.WT or RNA.122T or irrelevant RNA (Ctrl). **h**, Frequency of CAR T cells (CD45.1$^+$GFP$^+$) within T cells (left) and frequency of CAR T cells that had divided (CTV$^-$) within CAR T cells (right) in spleens of mice 5 days after vaccination. Significance was determined using an unpaired two-tailed Student's *t*-test. **i**, Serum ALT and AST levels 5 days after vaccination. Significance was determined using an unpaired two-tailed Student's *t*-test. **j**, Quantification of cleaved caspase 3 staining by IHC in livers of mice 5 days after vaccination. Significance was determined using an unpaired two-tailed Student's *t*-test. **k**, Cleaved caspase 3 staining in liver sections obtained 5 days after RNA-LNP injection. Representative images are shown. Yellow arrowheads highlight selected caspase 3$^+$ cells. Scale bars, 50 µm. **l**, Quantification of T cell infiltration by IHC in livers of mice 5 days after vaccination ($n = 10$ ROIs from $n = 4$ mice per group). The central line indicates the median and box edges show the interquartile range. Significance was determined using an unpaired two-tailed Student's *t*-test. Error bars indicate the mean ± s.e.m. Panels **a** and **g** created in BioRender; Baccarini, A. https://biorender.com/1x1s0aw (2026).

and schedule, resulting solely from silencing antigen expression in hepatocytes.

As i.v. injected RNA-LNPs are being used for cancer vaccines, we tested whether hepatocyte expression might influence therapeutic vaccine response. We implanted mice with A20 lymphoma cells expressing GFP as a model tumor-associated antigen (TAA)[36] (Fig. 4c). We subsequently vaccinated them with i.v. injections of mCherry RNA (negative control), GFP RNA.WT or GFP RNA.122T (in LNPs). Treatment with GFP RNA.WT led to a decrease in tumor growth compared to control (mCherry), demonstrating that TAA mRNA vaccination promoted tumor control (Fig. 4d,e). Notably, GFP RNA.122T led to an even greater reduction in tumor burden, with tumor volume lowered by >50%, just by detargeting TAA expression from hepatocytes (Fig. 4d,e). The frequency of GFP-specific intratumoral CD8$^+$ T cells was higher in the RNA.122T-vaccinated mice and doubled in the spleen (Fig. 4f,g). Both the intratumoral and splenic TAA-specific CD8 T cells had a less exhausted phenotype in animals vaccinated with RNA.122T (Fig. 4h,i), with a reduced frequency and expression level of PD1 and TIM3 on the TAA-specific T cells. Intratumoral CD8$^+$ T cells of RNA.122T-vaccinated mice also demonstrated increased activation and effector function, measured by expression of CD44, IFNγ and granzyme B (Fig. 4j,k).

To determine whether mRNA expression by hepatocytes dampens antigen-specific CD8$^+$ T cell response through the PD1/PDL1 pathway, we i.v. vaccinated mice with two doses of GFP RNA.WT or RNA.122T and treated with anti-PD1 or isotype control antibody between the two doses. With control antibody, we once again found that RNA.122T induced more antigen-specific T cells. Instead, in mice treated with anti-PD1, the difference in antigen-specific T cells was abolished between RNA.WT and RNA.122T (Fig. 4l,m).

These results indicate that LNP-delivered mRNA expression within hepatocytes suppresses the CD8$^+$ T cell response to the RNA-encoded antigen and suggests that detargeting hepatocytes may improve RNA vaccine responses.

RNA-LNPs can trigger hepatocyte damage by antigen-specific T cells, which is ameliorated by 122T

RNA vaccines are also being used to expand antigen-specific CAR or T cell receptor (TCR)-transgenic T cells. In this case, persons with adoptively transferred antigen-specific T cells are subsequently injected with an RNA encoding the target antigen[37]. RNA drugs are also used to express proteins such as Cas9, which many people have preexisting T cells against[38,39]. We sought to better understand how RNA-LNP cell expression patterns influenced the response of preexisting T cells. To

Fig. 6 | 133T and 206T silence mRNA expression in muscle fibers and reduce T cell expansion. a, Imaging of GFP expression in muscle 24 h after i.m. injection of 5 µg of GFP RNA.WT, RNA.133T.206T or PBS. Representative images are shown ($n = 3$ mice per group, from 3 independent experiments). Selected cells expressing GFP are indicated by yellow arrowheads. Scale bars, 100 µm. **b**, Imaging of GFP, macrophages (F4/80) and endothelial cells (CD31) in the muscle of mice injected as in **a**. White arrowheads highlight selected CD31$^+$ cells and yellow arrowheads highlight selected F4/80$^+$ cells. Scale bars, 50 µm. **c**, Imaging of GFP expression in the spleen from mice in **a**. Representative images are shown. Scale bars, 200 µm. **d**, Flow cytometry analysis of GFP$^+$ immune cell subsets in the spleens of mice from **a**. Values are plotted as a proportion of transfected cells for each respective cell type. Error bars indicate the mean ± s.d. **e**, Mice were i.m. injected on days 0, 5 and 20 with PBS or 5 µg of GFP-encoding RNA.WT or RNA.133T.206T ($n = 4$ mice per group, from 3 independent experiments). Anti-GFP IgG antibody titers were assessed in sera obtained 2 weeks after the priming dose of GFP RNA.WT or RNA.133T.206T LNPs. Error bars indicate the mean ± s.e.m. and the limit of detection is indicated by a dotted line. **f**, Frequency of GFP-specific CD8$^+$ T cells within CD8$^+$ T cells in the spleen 5 days after the third dose was measured by flow cytometry using $GFP_{200–208}$ H-2Kd tetramer from mice in **e**. Representative flow plots (left) and a graph of the mean ± s.e.m. (right) are shown, where each dot represents an individual mouse. **g**, Frequency of CD69$^+$ cells among GFP-specific CD8$^+$ T cells in the spleen from **e**. Error bars indicate the mean ± s.e.m. **h**, Quantification of granzyme B$^+$ splenic CD8$^+$ T cells upon in vitro stimulation with $GFP_{200–208}$ peptide-pulsed APCs ($n = 3$ mice per group). Error bars indicate the mean ± s.e.m. **i**, C57BL/6 mice ($n = 4$ per group) were i.m. injected with 2 doses of 5 µg of Spike RNA.WT or RNA.133T.206T or PBS 21 days apart. The fraction of Spike-specific CD8$^+$ T cells within CD8$^+$ T cells in the spleen 5 days after boost was measured by flow cytometry using $Spike_{539–546}$ H-2Kb tetramer. Error bars indicate the mean ± s.e.m. **j**, Quantification of granzyme B$^+$ (left) and Ki67$^+$ (right) spleen CD8$^+$ T cells from mice in **i** upon in vitro stimulation with Spike peptide-pulsed APCs. Error bars indicate the mean ± s.e.m. **k**, C57BL/6 mice were injected with 5 µg of GFP RNA.WT and injected muscle was obtained 24 h later ($n = 3$ mice per group). Multiplex IHC imaging was performed on muscle tissue sections for GFP (green), F4/80 (red) and MHC-I (magenta) (colored by pseudofluorescence). ROI-1 is adjacent to the injection site and ROI-2 is distant from the injection site within the same muscle. Individual channels and merged images are shown for each ROI. An uninjected control section is included for comparison. Scale bar, 20 µm. Significance was determined using an unpaired two-tailed Student's *t*-test.

https://doi.org/10.1038/s41587-026-03099-z

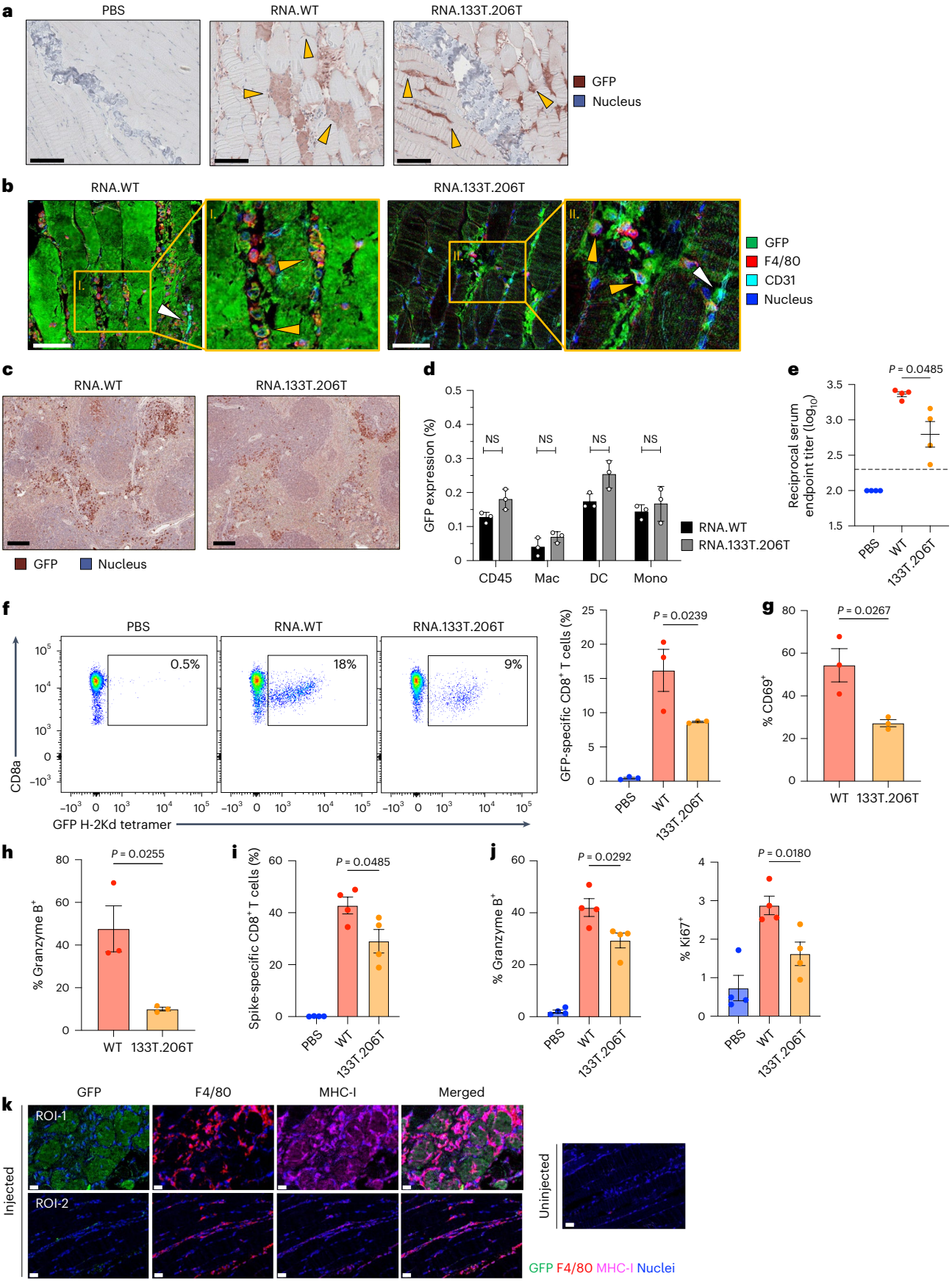

do this, we used Jedi T cells[40], which express a TCR specific for $GFP_{200–208}$ presented on MHC-I. We transplanted Jedi T cells into mice and, on the following day, i.v. injected 20 µg of GFP RNA.WT, RNA.122T or RNA.142T in LNPs (Fig. 5a). Examination of the liver indicated that RNA.WT led to a major infiltration of $CD8^+$ T cells in the tissue, with an average of 1,100 $CD8^+$ T cells per mm^2 (Fig. 5b,c). This was concomitant with an elevation in alanine transaminase (ALT) and aspartate transaminase (AST) in the serum, a measure of hepatocyte death (Fig. 5d). Instead, RNA.122T led to a major reduction in $CD8^+$ T cells in the liver and significantly lower ALT and AST in the serum. Expansion of Jedi T cells in the spleen was higher in RNA.122T-injected mice compared to RNA.WT, further indicating that hepatocyte expression of the payload limits T cell expansion (Fig. 5e,f).

We assessed whether this might occur with an RNA vaccine used to boost CAR T cells, which recognize antigens through antibodies rather than TCRs and have ~10-fold higher target requirements than TCRs[41–45]. Human CD19 (hCD19) CAR T cells were transferred into lymphodepleted mice (Fig. 5g,h) and the mice were subsequently vaccinated with RNA.WT or RNA.122T encoding hCD19. In two of four mice treated with RNA.WT, ALT rose above 400, whereas in untreated and RNA.122T-treated mice, ALT remained below 200 U per L (Fig. 5i). The livers of mice injected with RNA.WT also had significantly more apoptotic cells, indicated by caspase 3 cleavage (Fig. 5j,k) and a greater degree of T cell infiltration compared to RNA.122T (Fig. 5l).

These results suggest that injection of RNA-LNPs can lead to killing of hepatocytes by antigen-specific T cells and this can be prevented by inclusion of 122T.

133Ts and 206Ts silence mRNA expression in muscle fibers in vivo

The i.m. injection of RNA-LNPs leads to expression in muscle fibers (Extended Data Fig. 2) but it is not known whether muscle fiber expression has any effect, beneficial or deleterious, on RNA vaccine immunity. To investigate this, we first aimed to generate an mRNA not expressed in muscle fibers. We generated GFP-encoding RNA.133T.206T, which contained miRTs for the muscle-specific miRNAs miR-133 and miR-206 (ref. 16). We i.m. injected 5 µg of GFP RNA.133T.206T or RNA.WT (in LNPs) into the tibialis anterior muscle of mice and analyzed tissue after 18 h. Whereas injection of GFP RNA.WT led to expression in muscle fibers, we could not detect any GFP^+ muscle fibers in animals injected with RNA.133T.206T (Fig. 6a). This was specific for muscle fibers, as both formulations resulted in comparable GFP expression in muscle interstitial cells, which included macrophages and endothelial cells (Fig. 6b), and in hematopoietic cells of the spleen, including all pAPCs (Fig. 6c,d).

Muscle fiber expression contributes to the CD8 T cell response to mRNA-encoded protein

Next, we i.m. injected mice with 5 µg of GFP-encoding RNA.WT or RNA.133T.206T encapsulated in LNPs. We performed a prime and boost 5 days apart and then reboosted after 20 days. There was a very modest but consistent decrease in anti-GFP antibodies in RNA.133T.206T-treated mice (Fig. 6e). Notably, RNA.133T.206T led to a significant reduction in GFP-specific $CD8^+$ T cells, as indicated by tetramer staining (Fig. 6f). Moreover, when we isolated T cells from the mice and restimulated them with GFP-loaded APCs, the T cells were qualitatively different, with fewer granzyme B^+ and $CD69^+$ GFP-specific T cells from RNA.133T.206T-vaccinated animals (Fig. 6g,h).

To determine whether myocytes influence immunity to a real-world antigen, we primed and boosted mice with Spike RNA.WT or RNA.133T.206T through i.m. injection. The titer of Spike-specific IgG was equivalent between formulations, indicating that antibody induction was not affected and confirming matched dosing (Extended Data Fig. 7a,b). After priming, Spike-specific $CD8^+$ T cell levels were similar in the blood of both cohorts. However, after the boost, we once again found that silencing RNA in myocytes significantly decreased antigen-specific T cell expansion, with ~30% fewer Spike-specific T cells detected (Fig. 6i,j). This is quite remarkable considering that there was no significant difference in the quantity of Spike-specific CD8 T cells induced by vaccination with RNA.142T compared to RNA.WT (Fig. 3d,e). This means that direct expression of antigens in myocytes had a similar or greater impact on antigen-specific CD8 T cell induction compared to intrinsic RNA expression in pAPCs. The contribution of myocytes was additionally confirmed with a third antigen, OVA, in C57BL/6 mice (Extended Data Fig. 8). Our results demonstrate that direct expression of RNA-LNPs in muscle fibers contributes to the magnitude of the antigen-specific T cell response.

We wondered whether muscle fibers may be able to present antigens, as we and others have reported low MHC-I expression in the muscle in steady state[46]. Indeed, we did not detect MHC-I protein expressed by muscle cells at uninjected sites. However, in muscle injected with the GFP-encoding mRNA-LNPs, MHC-I was upregulated across the tissue, including on macrophages and GFP^+ muscle fibers (Fig. 6k). This suggests that muscle fibers are capable of presenting RNA-derived antigens to $CD8^+$ T cells and this may contribute to antigen-specific T cell expansion from i.m. injection of RNA-LNPs.

Discussion

Here, we show that LNP-delivered mRNA expression in non-APCs, specifically myocytes and hepatocytes, can impact the payload-specific T cell response as much as or more than direct expression in pAPCs. Notably, by silencing mRNA in hepatocytes, using 122T, there was a stronger T cell response, which translated to improved mRNA vaccine control of tumor growth.

Silencing mRNA expression in DCs did not diminish T cell priming and, in the case of Spike, did not even reduce the magnitude of CD8 T cell expansion or antibody titers. Our findings do not negate the importance of DCs in mRNA vaccine immunity, but they do indicate direct mRNA expression in DCs is not necessary. Indeed, we found that pAPCs, including DCs, were acquiring antigen from nonhematopoietic cells transfected by the RNA-LNP. Thus, it is likely that the pAPCs that acquired antigen were responsible for T cell priming through cross-presentation. It is notable how dispensable direct mRNA expression in DC was, as even though some exogenous antigen acquisition by DCs and other pAPCs may be expected, a key motivation for mRNA vaccines is that direct expression would lead to more efficient MHC-I loading than by cross-presentation. A possible explanation for this is that transfected DCs have impaired capacity to present, as described for virus infected DCs[47]. Indeed, Mellman and colleagues reported that cross-presentation by uninfected DCs of even small quantities of endocytosed influenza antigen was 300-fold more efficient than flu antigen presentation by infected DC[48]. Our findings revise our understanding about how mRNA vaccines work and have implications for their design, as well as the design of mRNA therapeutics.

Notably, silencing mRNA in muscle fibers decreased antigen-specific T cell expansion to a similar or greater degree compared to silencing in pAPCs. This was surprising because muscle fibers are not major APCs. They do not migrate to lymphoid tissue where naive T cells get primed and, in a steady state, they express low to undetectable levels of MHC-I (refs. 46,49), although we did observe that MHC-I was upregulated in mRNA-transfected muscle. Muscle fibers have been implicated in the efficacy of i.m. DNA and lentiviral vaccines[50–54], with extracellular vesicle (EV) release implicated[55]. However, it is not clear why antigen in myocytes would have such a strong impact on increasing the frequency of CD8 T cells (~30–50%) when there is so much direct expression in pAPCs from RNA-LNP injection. A possible explanation is that myocyte expression serves as a source of exogenous antigen for cross-presentation by DCs and this is a more potent mechanism of CD8 T cell activation than direct presentation by transfected DCs, as suggested by flu studies[47,48]. It may also be that skeletal muscle retains

antigen for longer and can serve as a reservoir of antigens to enable more continuous expansion of CD8 T cells.

An unanswered question is how antigens are transferred from transfected to nontransfected pAPCs. This could be through cell death (releasing free antigens or apoptotic bodies carrying antigens) or potentially through EV release. Surface shedding is another possibility and may account for why the T cell response to Spike and OVA, which are membrane bound, was less dependent on pAPC expression than GFP, which is cytoplasmic. Cross-dressing, involving transfer of peptide–MHC-I complexes from transfected cells to pAPCs, could be another mechanism, and suggested by recent work. More studies will be needed to determine this but our findings have implications for RNA-LNPs that are not intended for vaccination, as avoiding expression in APCs may not be sufficient to prevent immunity against the payload. Although the reduced magnitude of the response with intracellular antigen (GFP) suggests that it is still beneficial to include 142T in nonvaccine applications of mRNA therapeutics, such as for Cas9 expression, to detarget from pAPCs.

In contrast to muscle fibers, expression in hepatocytes suppressed the CD8 T cell response to mRNA-encoded antigen and silencing hepatic expression improved RNA vaccine efficacy in the lymphoma model. This suggests that, for RNA-LNP vaccines, especially those given i.v.[7], it is beneficial to detarget from hepatocytes when immunity is the objective and enhance hepatocyte expression when tolerance is the goal. The liver can promote tolerance through different mechanisms[56–58], including T cell deletion[59] or exhaustion[60] and the induction of regulatory T cells[56]. Our data suggest a role for the PD1/PDL1 pathways but we cannot rule out other mechanisms, nor can we rule out whether T cell dampening was mediated by direct presentation by hepatocytes or through transfer of antigen to pAPCs or liver sinusoidal endothelial cells.

We also demonstrate that adoptively transferred antigen-specific T cells kill cells expressing the mRNA-encoded antigens and this can be ameliorated by the inclusion of miRTs. This has implications for RNA vaccine boosting, including for expanding TCR-transgenic or CAR T cells. It is important to note that, in clinical studies of RNA vaccines, overt liver and muscle toxicity has not been reported and we stress that they have proven to be very safe. This includes a trial in which participants were given Claudin 6-specific CAR T cells and vaccinated with a Claudin 6-encoding mRNA[37]. In the latter, a lipoplex was used for mRNA delivery, which primarily delivers to DCs; thus, the number of antigen-expressing hepatocytes and other nonimmune cells may have been low. However, there may also be muscle or hepatocyte killing with RNA-LNP treatments in the repeat dose or CAR T cell setting that is difficult to detect but reduces the therapeutic index by limiting the dose ceiling. In this case, inclusion of miRTs for hepatocytes or other cell types could reduce organ infiltration and T cell killing of the cognate cells, as we demonstrated.

A major limitation of this study is that it is difficult to know how closely the functional biodistribution of mRNA-LNPs in animal models matches that in humans, as there is little characterization of the mRNA-LNP cellular expression patterns in humans, which will vary by LNP and mRNA formulation, dose, injection route and other factors[1]. The selected RNA-LNP formulation, dose and administration were guided by prior studies from different groups[7,61,62] and our studies were conducted in both C57BL/6 and BALB/c mice to demonstrate the applicability of miRTs for mRNAs encoding a diverse set of antigens[63]. However, we could not model all aspects of clinical applications and there are limitations of the animal models. Nevertheless, these studies provide general insights into how different cell types can affect the immune response to mRNA-encoded antigens.

As mRNA delivery efficiency and stability improve, including with self-amplifying and circular mRNA, the number of cell types expressing the mRNA will increase, as will the duration of time the protein payload remains in cells[64,65]. This will make it even more important to tailor mRNA expression and control immunity against the encoded payload. The use of miRTs provides a rational, robust and modular way to do this.

Online content

Any methods, additional references, Nature Portfolio reporting summaries, source data, extended data, supplementary information, acknowledgements, peer review information; details of author contributions and competing interests; and statements of data and code availability are available at https://doi.org/10.1038/s41587-026-03099-z.

References

1. Kang, D. D. et al. Targeting and tracking mRNA lipid nanoparticles at the particle, transcript and protein level. *Nat. Biomed. Eng.* **9**, 1591–1609 (2025).
2. Pardi, N., Hogan, M. J. & Weissman, D. Recent advances in mRNA vaccine technology. *Curr. Opin. Immunol.* **65**, 14–20 (2020).
3. Parhiz, H., Atochina-Vasserman, E. N. & Weissman, D. mRNA-based therapeutics: looking beyond COVID-19 vaccines. *Lancet* **403**, 1192–1204 (2024).
4. Dilliard, S. A. & Siegwart, D. J. Passive, active and endogenous organ-targeted lipid and polymer nanoparticles for delivery of genetic drugs. *Nat. Rev. Mater.* **8**, 282–300 (2023).
5. Pail, O., Lin, M. J., Anagnostou, T., Brown, B. D. & Brody, J. D. Cancer vaccines and the future of immunotherapy. *Lancet* **406**, 189–202 (2025).
6. Pardi, N., Hogan, M. J., Porter, F. W. & Weissman, D. mRNA vaccines—a new era in vaccinology. *Nat. Rev. Drug Discov.* **17**, 261–279 (2018).
7. Kranz, L. M. et al. Systemic RNA delivery to dendritic cells exploits antiviral defence for cancer immunotherapy. *Nature* **534**, 396–401 (2016).
8. Brown, B. D., Venneri, M. A., Zingale, A., Sergi Sergi, L. & Naldini, L. Endogenous microRNA regulation suppresses transgene expression in hematopoietic lineages and enables stable gene transfer. *Nat. Med.* **12**, 585–591 (2006).
9. Brown, B. D. et al. Endogenous microRNA can be broadly exploited to regulate transgene expression according to tissue, lineage and differentiation state. *Nat. Biotechnol.* **25**, 1457–1467 (2007).
10. Brown, B. D. et al. A microRNA-regulated lentiviral vector mediates stable correction of hemophilia B mice. *Blood* **110**, 4144–4152 (2007).
11. Brown, B. D. & Naldini, L. Exploiting and antagonizing microRNA regulation for therapeutic and experimental applications. *Nat. Rev. Genet.* **10**, 578–585 (2009).
12. Lockhart, J., Canfield, J., Mong, E. F., VanWye, J. & Totary-Jain, H. Nucleotide modification alters microRNA-dependent silencing of microRNA switches. *Mol. Ther. Nucleic Acids* **14**, 339–350 (2019).
13. Wroblewska, L. et al. Mammalian synthetic circuits with RNA binding proteins delivered by RNA. *Nat. Biotechnol.* **33**, 839–841 (2015).
14. Jain, R. et al. MicroRNAs enable mRNA therapeutics to selectively program cancer cells to self-destruct. *Nucleic Acid Ther.* **28**, 285–296 (2018).
15. Landgraf, P. et al. A mammalian microRNA expression atlas based on small RNA library sequencing. *Cell* **129**, 1401–1414 (2007).
16. Kelly, E. J., Hadac, E. M., Greiner, S. & Russell, S. J. Engineering microRNA responsiveness to decrease virus pathogenicity. *Nat. Med.* **14**, 1278–1283 (2008).
17. Mazzacurati, L. et al. Use of miRNA response sequences to block off-target replication and increase the safety of an unattenuated, glioblastoma-targeted oncolytic HSV. *Mol. Ther.* **23**, 99–107 (2015).
18. Miki, K. et al. Efficient detection and purification of cell populations using synthetic microRNA switches. *Cell Stem Cell* **16**, 699–711 (2015).

19. Breda, L. et al. In vivo hematopoietic stem cell modification by mRNA delivery. *Science* **381**, 436–443 (2023).
20. Karikó, K., Buckstein, M., Ni, H. & Weissman, D. Suppression of RNA recognition by Toll-like receptors: the impact of nucleoside modification and the evolutionary origin of RNA. *Immunity* **23**, 165–175 (2005).
21. Karikó, K. et al. Incorporation of pseudouridine into mRNA yields superior nonimmunogenic vector with increased translational capacity and biological stability. *Mol. Ther.* **16**, 1833–1840 (2008).
22. Parr, C. J. C. et al. N^1-Methylpseudouridine substitution enhances the performance of synthetic mRNA switches in cells. *Nucleic Acids Res.* **48**, e35 (2020).
23. Rose, S. A. et al. A microRNA expression and regulatory element activity atlas of the mouse immune system. *Nat. Immunol.* **22**, 914–927 (2021).
24. Hassett, K. J. et al. Optimization of lipid nanoparticles for intramuscular administration of mRNA vaccines. *Mol. Ther. Nucleic Acids* **15**, 1–11 (2019).
25. Mullokandov, G. et al. High-throughput assessment of microRNA activity and function using microRNA sensor and decoy libraries. *Nat. Methods* **9**, 840–846 (2012).
26. Reis e Sousa, C. Dendritic cells in a mature age. *Nat. Rev. Immunol.* **6**, 476–483 (2006).
27. O'Connell, R. M., Taganov, K. D., Boldin, M. P., Cheng, G. & Baltimore, D. MicroRNA-155 is induced during the macrophage inflammatory response. *Proc. Natl Acad. Sci. USA* **104**, 1604–1609 (2007).
28. Santiago, L. M. et al. WNT7A mRNA lipid nanoparticles promote muscle hypertrophy and reduce fatty infiltration. *Cell. Mol. Bioeng.* **18**, 387–401 (2025).
29. Lindsay, K. E. et al. Visualization of early events in mRNA vaccine delivery in non-human primates via PET-CT and near-infrared imaging. *Nat. Biomed. Eng.* **3**, 371–380 (2019).
30. Cheng, Q. et al. Selective organ targeting (SORT) nanoparticles for tissue-specific mRNA delivery and CRISPR–Cas gene editing. *Nat. Nanotechnol.* **15**, 313–320 (2020).
31. Verbeke, R., Hogan, M. J., Loré, K. & Pardi, N. Innate immune mechanisms of mRNA vaccines. *Immunity* **55**, 1993–2005 (2022).
32. Shortman, K., Lahoud, M. H. & Caminschi, I. Improving vaccines by targeting antigens to dendritic cells. *Exp. Mol. Med.* **41**, 61–66 (2009).
33. Alameh, M.-G. et al. Lipid nanoparticles enhance the efficacy of mRNA and protein subunit vaccines by inducing robust T follicular helper cell and humoral responses. *Immunity* **54**, 2877–2892 (2021).
34. Tahtinen, S. et al. IL-1 and IL-1ra are key regulators of the inflammatory response to RNA vaccines. *Nat. Immunol.* **23**, 532–542 (2022).
35. Brown, B. D., Fauci, A. S., Belkaid, Y. & Merad, M. RNA vaccines: a transformational advance. *Immunity* **56**, 2665–2669 (2023).
36. Upadhyay, R. et al. A critical role for Fas-mediated off-target tumor killing in T-cell immunotherapy. *Cancer Discov.* **11**, 599–613 (2021).
37. Mackensen, A. et al. CLDN6-specific CAR-T cells plus amplifying RNA vaccine in relapsed or refractory solid tumors: the phase 1 BNT211-01 trial. *Nat. Med.* **29**, 2844–2853 (2023).
38. Charlesworth, C. T. et al. Identification of preexisting adaptive immunity to Cas9 proteins in humans. *Nat. Med.* **25**, 249–254 (2019).
39. Wagner, D. L. et al. High prevalence of *Streptococcus pyogenes* Cas9-reactive T cells within the adult human population. *Nat. Med.* **25**, 242–248 (2019).
40. Agudo, J. et al. GFP-specific CD8 T cells enable targeted cell depletion and visualization of T-cell interactions. *Nat. Biotechnol.* **33**, 1287–1292 (2015).
41. Teppert, K. et al. Joining forces for cancer treatment: from 'TCR versus CAR' to 'TCR and CAR. *Int. J. Mol. Sci.* **23**, 14563 (2022).
42. Salter, A. I. et al. Comparative analysis of TCR and CAR signaling informs CAR designs with superior antigen sensitivity and in vivo function. *Sci. Signal.* **14**, eabe2606 (2021).
43. Harris, D. T. et al. Comparison of T cell activities mediated by human TCRs and CARs that use the same recognition domains. *J. Immunol.* **200**, 1088–1100 (2018).
44. Anikeeva, N. et al. Efficient killing of tumor cells by CAR-T cells requires greater number of engaged CARs than TCRs. *J. Biol. Chem.* **297**, 101033 (2021).
45. Sykulev, Y., Joo, M., Vturina, I., Tsomides, T. J. & Eisen, H. N. Evidence that a single peptide–MHC complex on a target cell can elicit a cytolytic T cell response. *Immunity* **4**, 565–571 (1996).
46. Agudo, J. et al. Quiescent tissue stem cells evade immune surveillance. *Immunity* **48**, 271–285 (2018).
47. Langlois, R. A., Varble, A., Chua, M. A., García-Sastre, A. & tenOever, B. R. Hematopoietic-specific targeting of influenza A virus reveals replication requirements for induction of antiviral immune responses. *Proc. Natl Acad. Sci. USA* **109**, 12117–12122 (2012).
48. Smed-Sörensen, A. et al. Influenza A virus infection of human primary dendritic cells impairs their ability to cross-present antigen to CD8 T cells. *PLoS Pathog.* **8**, e1002572 (2012).
49. Wiendl, H. et al. Antigen processing and presentation in human muscle: cathepsin S is critical for MHC class II expression and upregulated in inflammatory myopathies. *J. Neuroimmunol.* **138**, 132–143 (2003).
50. Coban, C., Kobiyama, K., Jounai, N., Tozuka, M. & Ishii, K. J. DNA vaccines: a simple DNA sensing matter? *Hum. Vaccin. Immunother.* **9**, 2216–2221 (2013).
51. Lin, Y.-Y. et al. Skeletal muscle is an antigen reservoir in integrase-defective lentiviral vector-induced long-term immunity. *Mol. Ther. Methods Clin. Dev.* **17**, 532–544 (2020).
52. Wolff, J. A., Ludtke, J. J., Acsadi, G., Williams, P. & Jani, A. Long-term persistence of plasmid DNA and foreign gene expression in mouse muscle. *Hum. Mol. Genet.* **1**, 363–369 (1992).
53. Bartlett, R. J. et al. Long-term expression of a fluorescent reporter gene via direct injection of plasmid vector into mouse skeletal muscle: comparison of human creatine kinase and CMV promoter expression levels in vivo. *Cell Transplant.* **5**, 411–419 (1996).
54. Loirat, D. et al. Muscle-specific expression of hepatitis B surface antigen: no effect on DNA-raised immune responses. *Virology* **260**, 74–83 (1999).
55. Wang, C., Cheng, X., Cheng, K. & Yuan, F. Extracellular vesicles are key mediators for direct antigen transport to draining lymph nodes. *Mol. Ther.* **34**, 606–619 (2026).
56. LoDuca, P., Hoffman, B. & Herzog, R. Hepatic gene transfer as a means of tolerance induction to transgene products. *Curr. Gene Ther.* **9**, 104–114 (2009).
57. Sack, B. K., Herzog, R. W., Terhorst, C. & Markusic, D. M. Development of gene transfer for induction of antigen-specific tolerance. *Mol. Ther. Methods Clin. Dev.* **1**, 14013 (2014).
58. Zheng, M. & Tian, Z. Liver-mediated adaptive immune tolerance. *Front. Immunol.* **10**, 2525 (2019).
59. Benseler, V. et al. Hepatocyte entry leads to degradation of autoreactive CD8 T cells. *Proc. Natl Acad. Sci. USA* **108**, 16735–16740 (2011).
60. Kumar, S. R. P., Hoffman, B. E., Terhorst, C., de Jong, Y. P. & Herzog, R. W. The balance between $CD8^+$ T cell-mediated clearance of AAV-encoded antigen in the liver and tolerance is dependent on the vector dose. *Mol. Ther.* **25**, 880–891 (2017).
61. Reinhard, K. et al. An RNA vaccine drives expansion and efficacy of claudin-CAR-T cells against solid tumors. *Science* **367**, 446–453 (2020).

62. DiPiazza, A. T. et al. COVID-19 vaccine mRNA-1273 elicits a protective immune profile in mice that is not associated with vaccine-enhanced disease upon SARS-CoV-2 challenge. *Immunity* **54**, 1869–1882 (2021).
63. Corbett, K. S. et al. SARS-CoV-2 mRNA vaccine design enabled by prototype pathogen preparedness. *Nature* **586**, 567–571 (2020).
64. Geall, A. J. et al. Nonviral delivery of self-amplifying RNA vaccines. *Proc. Natl Acad. Sci. USA* **109**, 14604–14609 (2012).
65. Chen, R. et al. Engineering circular RNA for enhanced protein production. *Nat. Biotechnol.* **41**, 262–272 (2023).

Methods

Materials

SM-102 was purchased from MedKoo Biosciences. Lipids 1,2-disteraroyl-*sn*-glycero-3-phosphocholine (DSPC), cholesterol and 1,2-dimyristoyl-*sn*-glycerol methoxypolyethylene glycol (DMG-PEG_{2000}) were purchased from Avanti Polar Lipids. Buffered formaldehyde (4%, J60401-AK) was purchased from Thermo Fisher Scientific. All mRNAs and modified RNAs used were produced using IVT[66]. All antibodies for flow cytometry were purchased from Thermo Fisher or Biolegend, as specified below. All antibodies for tissue histology were purchased from Thermo Fisher Scientific, Cell Signaling, Abcam or Takara, as specified below. Tetramer reagents were kindly provided by the National Institutes of Health (NIH) Tetramer Core Facility (Emory University Vaccine Center), as detailed below.

Cell lines

HEK293T, Phoenix-Eco, RAW264.7, MEL, AML12, 3T3, BCL1, C2C12 and HuH7 were obtained from the American Type Culture Collection (ATCC). GFP-A20 is a previously generated murine lymphoma cell line on the BALB/c background (H-$2K^d$) expressing eGFPP[36]. All cell lines were cultured at 37 °C with 5% CO_2 in the ATCC-recommended growth media. Cell lines were not independently authenticated aside from the identity provided by the ATCC. Cell lines were cultivated in a humidified incubator at 5% CO_2 and 37 °C. Cells were split at 70% confluency and tested for *Mycoplasma* quarterly.

Cloning of RNA template for IVT

Template plasmid with a T7 promoter site and codon-optimized eGFP were constructed by Twist Biosciences. Open reading frames (ORFs) contained restriction sites for the exchange of reporter gene constructs. Forward and reverse primers were used to amplify all reporter constructs. ORFs, UTRs and primer sequences are summarized in Supplementary Table 1. Templates for IVT were generated by restriction cloning using a T7 promoter sequence containing 5′UTR, an ORF and 3′UTR. Our construct used NASAR UTRs[67]. To construct miRNA-binding sites, we annealed two pairs of reverse and complementary oligonucleotides encoding 1–4 perfectly complementary target sites for a specific miRNA[9]. We then ligated the annealed oligonucleotide duplex into the IVT plasmid by cutting with BsrgI-HF (New England Biolabs (NEB), R3575) and SalI-HF (NEB, R3138) and ligated with T4 DNA ligase (NEB, 0202). Our design allowed us to encode four tandem miRTs and we could screen colonies for correct oligonucleotide insertion by inclusion of an MluI (NEB, R3198) restriction site, which only forms if oligos successfully anneal. The addition of a 120-nt poly(A) tail to the mRNAs was encoded on the PCR template with a reverse primer containing a 120-nt poly(T) sequence. To generate IVT template from plasmid, we amplified DNA with Q5 high-fidelity master mix (NEB, M0492). Following PCR, RNA was incubated at 37 °C for 30 min with DpnI (NEB, R0176) to remove plasmid contaminants and PCR product was cleaned up with the QIAquick PCR purification kit (Qiagen). Concentration was measured using a NanoDrop 2000 (Thermo Scientific) for application in IVT.

Synthesis and purification of mRNAs

All mRNAs were synthesized using the HiScribe T7 high-yield RNA synthesis kit (NEB) according to the manufacturer's instructions. Native mRNAs were synthesized with kit-supplied ATP, CTP, UTP and GTP. Modified nucleotides including N1m, ΨU and m5C were purchased from TriLink Biotechnologies and used as full substitutions of UTP or CTP in the reaction to synthesize modified mRNAs. Both mRNAs and modified mRNAs were capped by inclusion of a 1:4 premix of CleanCap reagent (TriLink) and capping occurred cotranscriptionally. The reaction mixtures were incubated at 37 °C for 5 h and further incubated at 37 °C for 30 min in the presence of TURBO DNase I (Thermo Scientific). RNA products were purified with the Monarch RNA cleanup kit (NEB, T2050). The RNA concentration was measured using a NanoDrop 2000 (Thermo Scientific) and species purity and size were assessed on a denaturing RNA gel.

Nanoparticle formation

RNA-loaded LNP formulations were formed using a microfluidic based mixing device (Ignite, Precision NanoSystems) for in vitro and in vivo studies. SM-102 particles[24] were formulated with the helper lipids (DSPC, cholesterol and DMG-PEG_{2000}; molar ratio 50:10:38.5:1.5) and mRNA or modified RNA dissolved in a citrate buffer. After formulation, the freshly formed RNA-LNPs were dialyzed overnight against PBS buffer using Slide-A-Lyzer dialysis cassettes (3.5-kDa molecular weight cutoff (MWCO); Life Technologies) and subsequently concentrated in Amicon Ultra centrifugal filters (10-kDa MWCO; Sigma) to the desired concentration. The particle size and zeta potential of LNPs were measured using a Zetasizer Advance (Malvern Panalytical) at a scattering angle of 173° and a temperature of 25 °C. The encapsulation efficiency of LNPs was determined using a Quant-it RiboGreen RNA assay kit according to manufacturer protocols. To quantify the RiboGreen assay, we used the Cytation 3 cell imaging reader (BioTek). Empty LNPs were formulated without mRNA in the aqueous phase. To label LNPs, DiI stain was added to the lipid mix at a 1:1,000 dilution before mRNA encapsulation. All formulations were within the following parameters: average size of 80–100 nm, encapsulation > 90% and polydispersity < 0.2.

Cloning of CAR constructs

An SFG-h1928z vector (hCD19 CAR) was constructed by stepwise Gibson assembly using the cDNA of a previously described anti-hCD19 scFv Myc-tag sequence (EQKLISEEDL), the murine CD28 transmembrane and intracellular domain and the murine CD3z intracellular domain into an SFG retroviral vector[68]. A GFP moiety, separated from the CAR by a T2A self-cleaving peptide, was cloned downstream of the CAR coding region[69]. CAR expression was verified by flow cytometry identification of GFP^+ cells.

Retroviral vector production

Phoenix-Eco cells were seeded into 15-cm tissue culture plates (Thermo Fisher Scientific, Nuclon, 168381) 24 h beforehand to achieve an approximate cell density of 70% at the moment of transfection. Transfection was carried out using the calcium phosphate method, as described previously[69]. Briefly, hCD19 CAR or control plasmid constructs were suspended in 0.1× TE (Maxi Qiagen kit, 12362) and 0.25 M $CaCl_2$ (Sigma-Aldrich, C7902-1KG) and one volume of 2× HBS (for 500 ml: 1 M HEPES (50 ml; Corning, 25-060-Cl), 2 M NaCl (70.25 ml; Fisher Bioreagents, BP358–1) and 0.5 mol l^{-1} Na_2HPO_4 (1.5 ml; Fisher Bioreagents, BP332–500)). Then, 378.25 ml of tissue-culture-tested water (Corning, 46–000-CV), supplemented with 5 M NaOH (Thermo Fisher, 134070010) to the desired pH, was added in dropwise fashion while continually vortexing and the resulting solution was immediately added to Phoenix-Eco cells and allowed to sit overnight. DMEM (Gibco, 11-965-118) was replaced the next morning; supernatants were collected and passed through a 0.22-µm filter 24–30 h later. Supernatant aliquots were stored at −80 °C until use.

hCD19 CAR T cell generation

CAR T cells were generated as previously[69]. Briefly, naive T cells were isolated from the spleens of CD45.1 C57BL/6 mice using the EasySep mouse T cell isolation kit (StemCell Technologies, 19851). Activation was carried out at a cell density of 1×10^6 cells per ml in RPMI medium + 100 U per ml recombinant murine IL-2 (Peprotech 212-12). Mouse T-activator CD3/CD28 Dynabeads (Thermo Fisher Scientific, 11453D) were used to activate cells at a 1:4 bead-to-cell ratio for 24 h before transduction. Nontreated culture plates (Nunc, Thermo Fisher Scientific) were coated overnight at 4 °C with 20 µg ml^{-1} RetroNectin (Takara, T100B). hCD19

CAR vector supernatant (see above) was spun for 90 min at 2,000*g* and 30 °C onto the plated RetroNectin and half the supernatant volume was removed carefully after spinning. T cells were resuspended in fresh RPMI medium with IL-2, added to the supernatant-containing wells (final IL-2 concentration of 50 U per ml) and allowed to sit for 24 h. After this, Dynabeads were magnetically removed and T cells were resuspended in fresh RPMI medium at 50 U per ml IL-2. New RPMI medium containing 50 U per ml IL-2 was added daily to keep T cells at a concentration between 1×10^6 and 2.5×10^6 cells per ml until use, within 5 days of isolation. Detection of GFP by flow cytometry was used to quantify the efficiency of transduction.

In vitro cell transfection and fluorescence detection

Cells were plated at 5×10^5 cells per well in a clear-bottom tissue culture plate. After 24 h, the medium in each well was replaced with 100–500 µl of medium containing modified RNA-LNPs. After 18 h, the cells were collected in flow tubes and cell fluorescence was measured using a LSRFortessa-X20 flow cytometer (BD Biosciences). To test the effect of miRT inclusion into Cas9-mRNA, Cas9-mRNA (original sequence purchased from Addgene, plasmid 42230) was coencapsulated into LNPs with β2-microglobulin single guide RNA (Synthego, 5′-GAGTAGCGCGAGCACAGCTAAGG-3′) at a mass ratio of 2.5:1. The 293T cells were plated at a concentration of 1.2×10^5 cells per well of a 24-well plate and transfected with 1 µg ml^{-1} of RNA-LNPs after 24 h. After 4 days of culture, cells were detached and stained for 30 min on ice with APC anti-human β2-microglobulin antibody (Biolegend, 395712) diluted 1:200 in FACS buffer (PBS with 2% FBS and 0.5 mM EDTA). Cells were then acquired with BD FACSDiva software on an LSRFortessa-X20 (BD Biosciences). The effect of miR-122 antagomiR on the expression of GFP mRNA was tested on HuH7 cells. Cells were plated at a concentration of 1×10^5 cells per well in a 24-well plate. After 24 h, each well was transfected with different amount of miR-122 antagomiR using Lipofectamine 3000 transfection reagent (Thermo Fisher, L3000015), according to manufacturer instructions. Then, 6 h after antagomiR transfection, cells were treated with 1 µg ml^{-1} of LNP-encapsulated GFP RNA.WT or RNA.122T. Cells were acquired 18 h after LNP transfection with BD FACSDiva software on an LSRFortessa-X20 (BD Biosciences). Bone-marrow-derived DCs were differentiated from the bone marrow of BALB/c mice using GM-CSF and plated at a concentration of 6.25×10^5 cells per ml. After 3 h, each well was transfected with 1 µg ml^{-1} mRNA encapsulated in DiI-stained LNP. Supernatant was collected 24 h after LNP transfection for Olink analysis. Cells were sorted for expression of DiI on a FACSymphony S6 (BD Biosciences).

RT–qPCR

Total RNA was extracted from each sample using QIAzol lysis reagent (Qiagen) and cDNA was synthesized from the isolated RNA with the iScript cDNA synthesis kit (Bio-Rad). Transcript levels of *Il10*, *Il6*, *Il12*, *Tnf* and *Il1b* were measured by qPCR using the SsoAdvanced Universal SYBR green supermix (Bio-Rad). *Gapdh* was used as the endogenous reference gene for normalization across all samples and the relative expression of the target genes in treatment groups compared to the control group was calculated using the $\Delta\Delta C_t$ method. All qPCR primers were purchased from Integrated DNA Technologies.

Mice

In vivo studies were performed using C57BL/6, BALB/c, Ai14 and B6.SJL-*Ptprc*^{a}*Pepc*^{b}/BoyJ (B6 CD45.1) mice obtained from the Jackson Laboratory (JAX, 000664, 000651, 007914 and 028062, respectively) and housed in the Mount Sinai vivarium during use. Jedi mice on a BALB/c background, derived from B10.D2 Jedi mice generated in the B.D.B. lab[40] by backcrossing. All mouse experiments were carried out under Institutional Animal Care and Use Committee (IACUC) approval. All mice were randomized before experimentation. For bone marrow transplantation experiments, lethally irradiated (11 Gy) Ai14 mice were reconstituted with 2×10^6 bone marrow cells from B6 CD45.1 or Ai14 mice. Mice were allowed to reconstitute for at least 8 weeks before use. Age-matched (6–12 weeks) female animals were used throughout all experiments. For studies of the CD8 T cell response to GFP, OVA or Spike, the strain choice was dictated by the availability of MHC-I-restricted tetramers, as described below. All experiments carried out at the Icahn School of Medicine at Mount Sinai were performed in compliance with federal laws and institutional guidelines and were approved by the IACUC (protocol no. IACUC-2018-0070).

Mouse injections and sample collections

For biodistribution experiments, C57BL/6 or Ai14 mice with weights of 18–20 g were injected with GFP RNA-LNPs or Cre RNA-LNPs. For i.v. administration, mice were injected with 20 µg (0.1 mg ml^{-1}) RNA-LNPs through the lateral tail vein, unless otherwise stated. For i.m. administration, mice were injected with 5 µg (0.1 mg ml^{-1}) RNA-LNPs in the left tibialis anterior muscle. At experimental endpoints, mice were killed and tissue was collected. In Ai14 experiments, mice were first imaged using whole-organ fluorescence with IVIS. In all experiments, organs were subsequently divided in two, with half processed as a cell suspension for flow cytometry and the other half fixed overnight in 4% PFA and paraffin-embedded for immunohistochemistry (IHC).

For vaccination experiments, mice were i.m. or i.v. injected as described above. At midpoint intervals between doses, blood was collected by retroorbital sampling using a sterile hematocrit capillary tube. For flow cytometry analysis of immune cells, blood was collected at 4 °C and processed as described below. For collection of serum, blood was incubated at 25 °C for 30 min to allow clotting and pelleted for 10 min at 2,000*g*. At experimental endpoints, mice were killed; blood and tissue were collected and processed for immune assays, as described below.

For tumor inoculation, GFP-A20 lymphoma cells[36] were passed through a 70-µm cell strainer and resuspended in ice-cold sterile PBS at a concentration of 10^7 cells per ml. A total of 10^6 cells were injected subcutaneously in a volume of 100 µl into the right back flank using a 27G needle. Mice were vaccinated with 20 µg of RNA-LNPs injected i.v. according to the schedule shown in respective figures. Tumor sizes were measured with a caliper every 2 or 3 days for calculating tumor volumes using the equation (width^2 × length)/2. Animals were killed when exhibiting signs of impaired health, when the tumor ulcerated or when the tumor volume exceeded 1,500 mm^3.

Adoptive cell transfer

Jedi T cell experiments were performed as previously described[46]. Briefly, donor spleen was collected from Jedi mice and processed into a single-cell suspension by mincing using a sterile blade, homogenizing by pipetting and filtering through a 70-µm cell strainer. The spleen solution was washed once with R10 medium and pelleted by centrifuging for 5 min at 400*g*. The supernatant was removed and the cell pellet was resuspended in 1 ml of 1× red blood cell (RBC) lysis buffer. After incubation, 10 ml of PBS was added to stop RBC lysis. The solution was centrifuged again at 400*g* for 5 min to obtain a cell pellet. A single-cell suspension was processed for isolation of CD8$^+$ T cells using the EasySep mouse CD8$^+$ T cell isolation kit (StemCell Technologies, 19853) as per the manufacturer's protocol. Isolated T cells were counted and suspended in sterile PBS to a concentration of 5×10^6 per ml. A total of 5×10^4 Jedi T cells were transplanted into Balb/c mice through i.v. injection into the retrobulbar venous plexus. After another 24 h, recipient mice were i.v. injected with 20 µg of GFP-encoding RNA-LNPs. Mice were killed at specified time points (24, 72 and 120 h) and blood and tissue were collected for immune analyses and tissue imaging.

For adoptive cell transfer of hCD19 CAR T cells, CAR-expressing CD45.1$^+$ T cells were incubated with CellTrace violet (CTV) according to the manufacturer's protocol and injected i.v. into the retrobulbar venous plexus into total-body-irradiated C57BL/6 recipient mice (4 Gy).

Then, 24 h later, mice received 20 µg of RNA-LNPs through i.v. injection. Mice treated with irrelevant antigen RNA-LNPs served as controls.

PD1 blockade

For immune checkpoint blockade, BALB/c mice were injected i.v. with a priming dose of 20 µg of GFP RNA-LNPs. Then, 5 days later, mice were injected intraperitoneally with 200 µg per dose of InVivoMAb anti-mouse PD1 (CD279) (clone RMP1-14; BioXCell, BE0146) or InVivoMAb rat IgG2a isotype control (BioXCell, BE0089) antibodies biweekly until they received a booster dose of 20 µg of GFP RNA-LNPs on day 21. The experiment endpoint was 5 days after the booster dose, at which point mice were killed and tissues samples were collected.

Whole-organ imaging

To measure whole-organ fluorescence of organs from Ai14 mice following Cre RNA-LNP injection, mice were first killed and then transcardiac perfused with 20 ml of PBS to remove blood, which would confound measurement of organ fluorescence. Indicated organs were collected on ice and fluorescence was measured (excitation: 550 nm and emission: 580 nm) using an IVIS imaging system (PerkinElmer) and quantified using LivingImage software (PerkinElmer). Tissue was subsequently processed for use in other analysis modalities as described below.

Tissue preparation

Peripheral blood was collected from the orbital sinus. A20 lymphoma tumors, spleens and LNs were collected in RPMI with 2% FBS on ice, homogenized by smashing using the plunger of a 3-ml syringe (BD Biosciences) and filtered through a 70-µm cell strainer. Erythrocytes for peripheral blood, spleens and tumors were removed using 1× RBC lysis buffer (Thermo, 00-4333-57). Bone marrow cells were flushed from femur and tibia bones, homogenized and filtered through a 70-µm cell strainer, before erythrocytes were removed by hypotonic lysis. For tissue preparation of livers, transcardiac perfusion with 10 ml of ice-cold PBS was first performed. Livers were collected in RPMI with 2% FBS on ice, minced using a sterile blade and digested with 1 mg ml^{-1} collagenase IV (Gibco, 17104019) and 40 µg ml^{-1} DNase I (Signma-Aldrich, DN25) dissolved in PBS with 5% FBS for 30 min at 37 °C with constant shaking. Liver homogenate was filtered through a 70-µm cell strainer. Cells were resuspended in 40% Percoll (Cytiva), previously adjusted with 10× PBS and layered onto 70% Percoll. The Percoll gradient was centrifuged at 400*g* for 25 min at 24 °C with no acceleration and no brake. The layer containing immune cells was collected and washed with FACS buffer (PBS with 2% FBS and 0.5 mM EDTA).

Flow cytometry

To assess expression of $tdTomato^+$ or GFP^+ cells in the different cell types of each organ, cell isolation and staining were performed after either day 1 or day 3 of treatment with RNA-LNPs followed by flow cytometry analysis. In all organs analyzed, after generating single-cell suspensions, samples were divided in two and stained with a lymphoid-specific panel or myeloid-specific panel of antibodies. Lineage-negative gates were included to exclude myeloid cells from lymphoid analysis and vice versa. All flow panels included a viability stain to discriminate live cells (live/dead fixable blue dead cell stain kit; L23105, Thermo Fisher). Single-cell suspensions were incubated in FACS buffer (PBS, 2% FBS and 0.5 mM EDTA) containing CD16/CD32 (Mouse Fc Block, BD) for 10 min before and during staining with extracellular antibodies. GFP-specific $CD8^+$ T cells were detected with H-$2K^d$/$GFP_{200–208}$ (HYLSTQSAL) tetramer, OVA-specific $CD8^+$ T cells with H-2Kb/$Ova_{257–264}$ (SIINFEKL) tetramer and SARS-CoV-2 Spike-specific $CD8^+$ T cells with SARS-CoV-2 $Spike_{539–546}$ (VNFNFNGL) tetramer, all kindly provided by the NIH Tetramer Core Facility (Emory University Vaccine Center). For tetramer staining, splenocytes or tumor cell suspensions were stained for 1 h at room temperature in the dark with tetramer and 50 nM dasitinib (StemCell Technologies, 73084). Viability stain with live/dead fixable blue stain (Thermo Fisher) was performed for 20 min at 4 °C, followed by staining for cell surface markers for 20 min at 4 °C.

Antibodies for extracellular staining included the following: from Biolegend, CD11b (M1/70, FITC and APC), FOLR2 (10/FR2, APC), XCR1 (ZET, APC–Cy7 and APC), MHC-II (M5/114.15.2, BV510), F4/80 (BM8, BV605), CD11c (N418, BV650), CD64 (X54-5/7.1, BV711 and PE), CD45 (30-F11, BV510, BV785 and Spark NIR 685), CD3 (17A2, Spark UV 387), CD4 (RM4-5, PE, BV605 and BV785), CD25 (PC61, PE/Dazzle594), CD44 (IM7, BV510), CD62L (MEL-14, BV570), TIM3 (RMT3-23, BV711), CD8a (53-6.7, BV785), CD69 (H1.2F3, APC–Cy7); from eBioscience, NKp46 (29A1.4, PerCP–eFluor 710), CD45.1 (A20, PE–Cy7), Ly6G (1A8–Ly6g, Alexa Fluor 700), Ly6C (HK1.4, eFluor450), PD1 (J43, PerCP–eFluor 710), CD3e (145-2C11, FITC), NK1.1 (PK136, APC–eFluor780), CD19 (eBio1D3, eFluor450), CD64 (10.1, PE–Cy7); from BD Bioscience, B220 (RA3-6B2, BUV563), CD8a (53-6.7, APC), Siglec-F (E50-2440, APC–Cy7) and CD25 (PC61, PE). Intracellular cytokine staining was performed with monoclonal antibodies to IFNγ (XMG1.2, PE–Cy7), and granzyme B (QA16A02, APC) from Biolegend, using the eBioscience intracellular fixation and permeabilization buffer set (Invitrogen, 88-8824-00) after stimulation of 2×10^6 splenocytes or tumor cells with 1 µM $GFP_{200–208}$ peptide, 1 µM SIINFEKL or Spike peptide pool (2 µg ml^{-1} per peptide) in the presence of brefeldin A (eBioscience 1000X solution) for 5 h at 37 °C. Transcription factor staining was performed with FoxP3 antibody from eBioscience (FJK-16s, PE–Cy7) using the FoxP3, transcription factor fixation and permeabilization concentrate and diluent kit (eBioscience). All intracellular staining was performed overnight at 4 °C. tdTomato fluorescence was detected in the PE channel and GFP fluorescence was detected in the FITC channel. Samples were acquired with BD FACSDiva software on a LSRFortessa-X20 (BD Biosciences) or Cytek SpectroFlo software on an Aurora 5L (Cytek) and analyzed with FlowJo (version 10.10.0).

Ex vivo uptake studies

For the ex vivo splenocyte culture, spleens from BALB/c mice were processed to a single-cell suspension as above. A total of 5×10^5 splenocytes were resuspended in R10 medium and transfected with 1 µg of RNA-LNPs. After 18 h, splenocytes were collected for flow cytometry to quantify GFP. For primary monocyte transfection, monocytes were isolated from the spleen using the Miltenyi Biotec monocyte isolation kit for mice (Miltenyi, 130-100-629) and cultured in nontissue-culture-treated plates at 5×10^5 cells per ml R10 medium supplemented with 40 ng ml^{-1} of M-CSF (PeproTech). The following day, cells were transfected with GFP-encoding RNA-LNPs. After 18 h, GFP expression was quantified by flow cytometry.

Multiplexed IHC consecutive staining on single slide

Iterative cycles of immunostaining on 5-µm-thick formalin-fixed paraffin-embedded (FFPE) tissue sections were performed as previously described[70]. Briefly, slides were baked overnight at 60 °C, then deparaffinized in xylene and rehydrated in descending series of 100%, 90%, 70% and 50% ethanol. Slides were incubated at 95 °C for 30 min in antigen retrieval solution (pH 9, Dako), cooled at room temperature and rinsed in Tris-buffered saline. Tissue endogenous peroxidase activity was quenched by a 15-min incubation in 3% H_2O_2 and slides were subsequently blocked with serum-free protein block (Agilent) for 30 min at room temperature. Tissue was stained with primary antibody diluted in background reducing antibody diluent (Agilent) for 1 h at room temperature, then washed three times and incubated with the horseradish-peroxidase-conjugated secondary antibody for 30 min at room temperature. Antigen detection was performed using the AEC peroxidase substrate kit (Vector Laboratories) and slides were counterstained with Harris-modified hematoxylin solution (Sigma-Aldrich). The slides were mounted in Glycergel mounting medium (Agilent) and imaged on an Aperio AT2 slide scanner (Leica) at ×40 magnification.

To perform the subsequent staining, the coverslip was removed by incubating the slides in 60 °C water and AEC and hematoxylin were removed in ascending series of 50%, 70% (with 1% HCl 12 N) and 100% ethanol. Sections were then rehydrated in descending series of 70% and 50% ethanol. From that point, the staining process continued iteratively, with a shortened antigen retrieval step (15 min at 95 °C). If two primary antibodies used consecutively were raised in the same species, an extra species-specific blocking step was performed with AffiniPure Fab fragment donkey anti-'species' IgG (Jackson Immuno Research). The following primary antibodies were used: anti-GFP (Takara, 632381), anti-DsRed (Takara, 632496), anti-F4/80 (Cell Signaling, 70076S), anti-CD31 (Abcam, ab182981), anti-CD8a (Cell Signaling, 98941S), anti-B220 (Thermo Fisher Scientific, 14-052-82), anti-LY6G (BioLegend, 127601), anti-αSMA (Abcam, ab5694), anti-MHC-I (Cell Signaling, 76828) and anti-cleaved caspase 3 (Cell Signaling, 9661).

Immunofluorescence tissue imaging

Flash-frozen unfixed mouse livers were embedded in OCT. Tissue was cryosectioned and mounted on slides with Fluoromount-G containing DAPI (Southern Biotech, 0100-20). The slides were blinded and immediately imaged with a Zeiss LSM780 fluorescence microscope.

Cyclic immunofluorescence

Cyclic immunofluorescence (CyCIF) was performed as previously described in detail[71,72]. Briefly, 5-µm-thick FFPE tissue sections were baked at 60 °C overnight, deparaffinized in xylene and rehydrated in decreasing concentrations of ethanol solutions (100%, 90%, 70% and 50%). Antigen retrieval was performed by incubating the slides in antigen retrieval solution (pH 9, Dako) at 95 °C for 30 min. Slides were then cooled at room temperature for 30 min and washed with PBS. Slides were photobleached by immersing them in a bleaching solution (4.5% H_2O_2 and 20 mM NaOH in PBS) with LED light exposure twice for 45 min to reduce autofluorescence. To mitigate nonspecific antibody binding, slides were washed three times for 5 min with 1× PBS and then incubated overnight with secondary antibodies (anti-rat, anti-mouse and anti-rabbit) diluted 1 in 1,000 in 150 µl of Odyssey blocking buffer at 4 °C in the dark. Slides were subsequently washed three times with 1× PBS before photobleaching them again twice for 45 min. For each round of CyCIF, samples were incubated overnight at 4 °C in the dark with Hoechst 33342 (1:10,000 dilution; Thermo Fisher Scientific) for nuclear staining along with either primary conjugated or primary unconjugated antibodies diluted in 150 µl of Odyssey blocking buffer (LI-Cor). Incubation with primary unconjugated antibodies was followed by secondary antibody incubation at room temperature for 2 h in the dark. Then, the slides were washed three times for 5 min and mounted with 200 µl of 70% glycerol. Slides were automatically imaged on the RareCyte Cytefinder II HT using the following channels: ultraviolet, Cy3, Cy5 and Cy7. Imaging was performed with the following parameters: binning, 1 × 1; objective, ×20; numerical aperture, 0.75; resolution, 0.325 µm per pixel. Image exposures were optimized for each channel to avoid signal saturation but kept constant across samples. After imaging, slides were placed in containers of 1× PBS and heated in a water bath for 1 h to remove coverslips. Between each cycle, slides were photobleached twice for 45 min and washed three times for 5 min in 1× PBS. The antibodies used in this panel were anti-MHC-I (Cell Signaling, 76828), anti-F4-80 (Cell Signaling, 70076S) and anti-CD8a (Cell Signaling, 98941s).

ELISA assays

To coat plates, 96-well polystyrene high-bind microplates (Corning, 3361) were incubated with recombinant *Aequorea victoria* GFP protein (Abcam, ab84191) at a concentration of 1 µg ml^{-1} at 4 °C overnight. Plates were washed and incubated in blocking buffer containing PBS with 5% milk and incubated for 1 h at 25 °C. Plates were incubated with serial dilutions of sera for 1 h at room temperature. Next, plates were washed and incubated with goat anti-mouse IgG(H + L) AP antibody (Southern Biotech, 1031-04) at a concentration of 1:2,000 in blocking buffer and incubated for 30 min at room temperature. Plates were washed one last time and the signal was detected with the AttoPhos AP fluorescent substrate system (Promega, PR-S1000). The plates were allowed to develop for 10 min and stopped with 3 N NaOH (Sigma). Plate fluorescence (excitation: 450 nm, emission: 580 nm and gain = 55) was measured with the Cytation 3 cell imaging reader (BioTek). To measure anti-Spike serum antibody titers, 96-well plates were coated with SARS-CoV-2 spike protein S1 (residues 14–683; Thermo Fisher, RP-87681) at a concentration of 2.5 µg ml^{-1} in PBS and incubated at room temperature overnight. Blocking was performed with 1% BSA, 1 mM EDTA and 0.05% Tween in PBS at room temperature for 2 h. The following steps were performed as previously described, with the only difference being the secondary antibody incubation that was extended to 1 h. In between each step, plates were washed three times with PBS and 0.05% Tween. Endpoint titers were calculated as the dilution that emitted fluorescence exceeding the background tenfold from negative control mice and extrapolated from a linear regression using R.

Olink proteomics

Cell culture supernatant and mouse serum samples were analyzed using the Olink proximity extension assay technology (Olink Proteomics). Samples were processed by the Human Immune Monitoring Center at Mount Sinai using the Target 96 mouse exploratory panel according to the manufacturer's instructions. Protein abundance is reported as normalized protein expression values on a $\log_2$ scale.

Quantification and statistical analysis

Statistical values including the number of replicates and statistical significance are reported in the figures or figure legends when appropriate. For the majority of in vivo experiments, the experiments were repeated at least two separate times with different cohorts of mice, synthesized RNAs and encapsulated and quantified RNA-LNPs. Statistical analysis was performed using Microsoft Excel, GraphPad Prism 10 (GraphPad Software) or R. Flow cytometry analysis was performed using FlowJo (version 10.10.0). The histology was processed, images were rendered and signal was quantified using QuPath and ImageJ software. The levels of significance (unpaired two-tailed Student's *t*-test) are denoted as $^{*}P < 0.05$, $^{**}P < 0.01$, $^{***}P < 0.001$ and $^{****}P < 0.0001$. Mechanistic schema and experimental schema were made using BioRender and Microsoft PowerPoint.

Reporting summary

Further information on research design is available in the Nature Portfolio Reporting Summary linked to this article.

Data availability

Raw data are provided in Supplementary Data 1. Source data are provided with this paper.

References

66. Vadovics, M., Muramatsu, H., Sárközy, A. & Pardi, N. Production and evaluation of nucleoside-modified mRNA vaccines for infectious diseases. *Methods Mol. Biol.* **2786**, 167–181 (2024).
67. Zeng, C. et al. Leveraging mRNA sequences and nanoparticles to deliver SARS-CoV-2 antigens in vivo. *Adv. Mater.* **32**, e2004452 (2020).
68. Davila, M. L., Kloss, C. C., Gunset, G. & Sadelain, M. CD19 CAR-targeted T cells induce long-term remission and B cell aplasia in an immunocompetent mouse model of B cell acute lymphoblastic leukemia. *PLoS ONE* **8**, e61338 (2013).
69. Sánchez-Paulete, A. R. et al. Targeting macrophages with CAR T cells delays solid tumor progression and enhances antitumor immunity. *Cancer Immunol. Res.* **10**, 1354–1369 (2022).

70. Dhainaut, M. et al. Spatial CRISPR genomics identifies regulators of the tumor microenvironment. *Cell* **185**, 1223–1239 (2022).
71. Lin, J. R. et al. Highly multiplexed immunofluorescence imaging of human tissues and tumors using t-CyCIF and conventional optical microscopes. *eLife* **7**, e31657 (2018).
72. Mollaoglu, G. et al. Ovarian cancer-derived IL-4 promotes immunotherapy resistance. *Cell* **187**, 7492–7510 (2024).

Acknowledgements

We thank members of the B.D.B. lab for their helpful comments, N. Bhardwaj, N. Vabret and D. Zamarin (Sinai) for discussions, and the Mount Sinai RNA Nanoparticle Core. B.D.B. and this work were supported by the NIH (R01DK138025 and R01CA257195) and the Feldman Family Foundation. Y.D. was supported by the NIH (U01EB035521). S.S. was supported by the NIH (F30AI194739). A.M. was supported by the NIH (T32AI078892). F.B. was supported by a Swiss National Science Foundation Fellowship. We thank the NIH Tetramer Core Facility (NIH contract 75N93020D00005 and RRID:SCR_026557) for providing all the tetramers used in this study.

Author contributions

Conceptualization, A.M., S.S. and B.D.B. Methodology, A.M., S.S., F.B., A.A., A.B., J.D.B. and B.D.B. Investigation, A.M., S.S., F.B., A.L., C.W., M.P., A.Z., C.M., J.M.-F., A.A., J.D.B. and Y.D. Writing—original draft, A.M., S.S. and B.D.B. Writing—review and editing, S.S., A.M., F.B., A.J.P.T., J.D.B., A.B., M.M., Y.D. and B.D.B. Supervision, B.D.B. Funding, M.M., Y.D. and B.D.B.

Competing interests

B.D.B. has a patent on the use of miRTs in gene vectors, which is not related to this work. B.D.B. is on the scientific advisory boards of Asgard Therapeutics, Noetik and Navexio and consults for Merck. Y.D. is a cofounder and holds equity in Immunanoengineering Therapeutics. The other authors declare no competing interests.

Additional information

Extended data is available for this paper at https://doi.org/10.1038/s41587-026-03099-z.

Supplementary information The online version contains supplementary material available at https://doi.org/10.1038/s41587-026-03099-z.

Correspondence and requests for materials should be addressed to Brian D. Brown.

Peer review information *Nature Biotechnology* thanks Bowen Li and the other, anonymous, reviewer(s) for their contribution to the peer review of this work.

https://doi.org/10.1038/s41587-026-03099-z

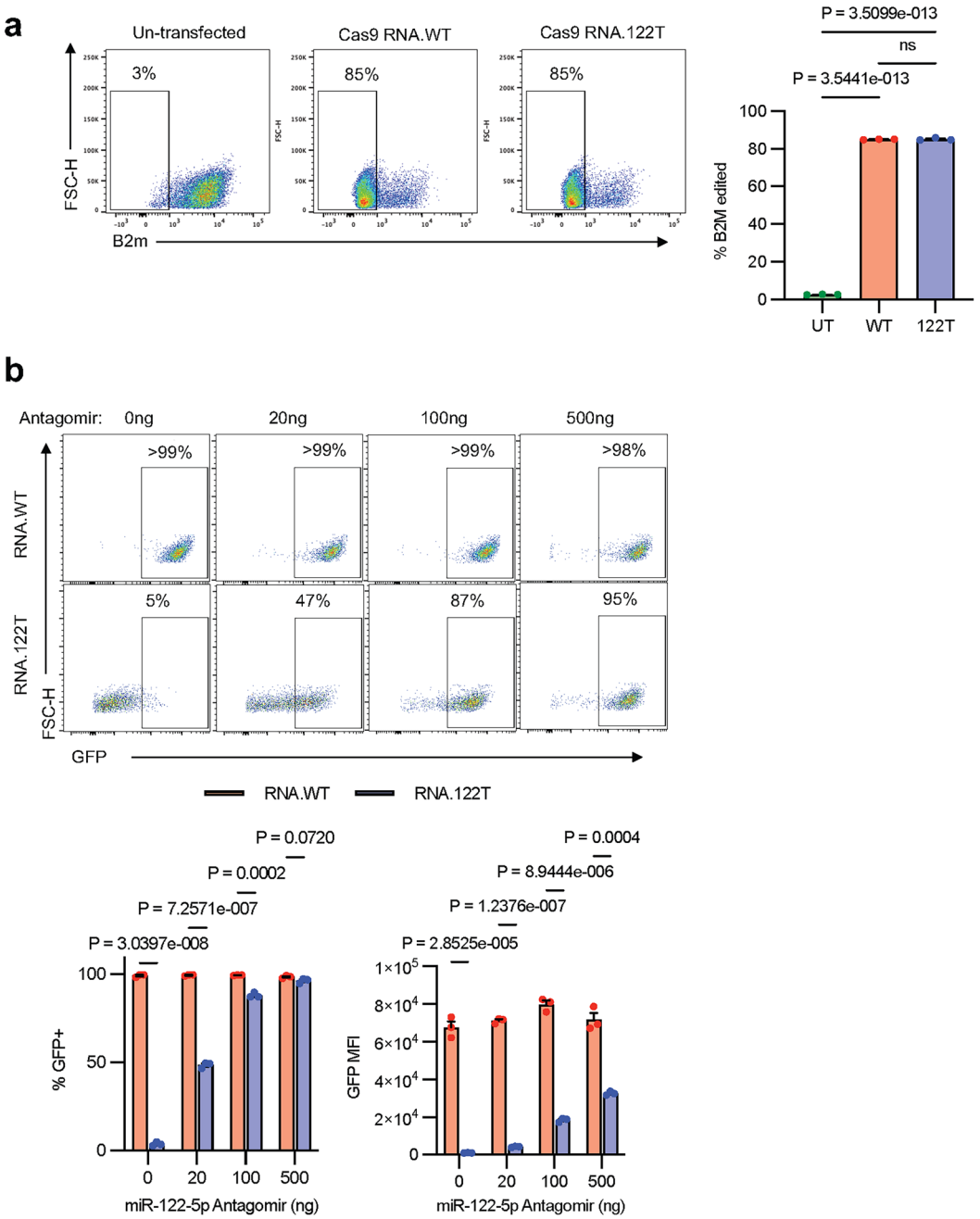

Extended Data Fig. 1 | RNA-LNP functional characterization and antagomiR-mediated blocking of miRNA activity. (**a**). HEK293T cells were transfected with LNP co-encapsulating Cas9 RNA.WT or RNA.122 T and sgRNA targeting *B2M* (1 µg RNA total; 2.5:1 ratio between Cas9 and *B2M* sgRNA). 4 days later, B2m expression was quantified by flow cytometry. (**b**). HuH7 cells were treated with anti-miR-122-5p antagomiR for 6 h, followed by transfection with 500 ng GFP RNA.WT or RNA.122T-LNP. Percentage and MFI of GFP expression was measured by flow cytometry, with representative flow plots shown. Data are presented as mean ± SEM. ns: not significant, analyzed by unpaired two-tailed Student's t-test (n = 3, independent wells of cells).

https://doi.org/10.1038/s41587-026-03099-z

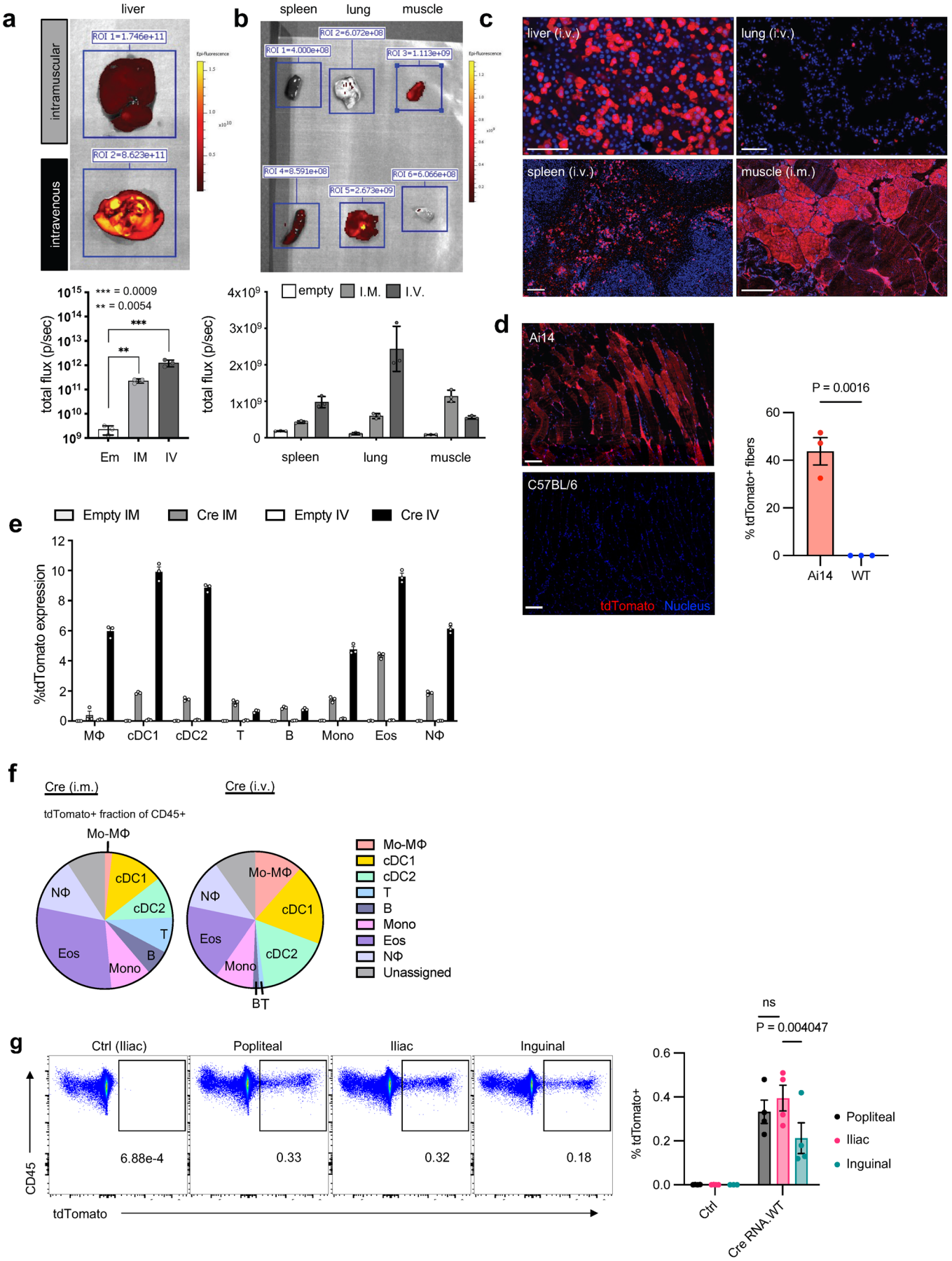

Extended Data Fig. 2 | See next page for caption.

https://doi.org/10.1038/s41587-026-03099-z

Extended Data Fig. 2 | RNA-LNP expression pattern following i.v. and i.m. delivery. (**a**). Whole organ imaging and quantification of mean fluorescence signal in liver following intramuscular (i.m.) and intravenous (i.v.) injection of Ai14 mice with Cre RNA-LNP. Graph shows the mean tdTomato signal intensity from the liver (n = 3 mice, repeated 3 independent times). Data are presented as mean ± SEM. Unpaired two-tailed Student's t-test comparison. (**b**). Whole organ fluorescence imaging and quantification of mean tdTomato signal in spleen, lung, and tibialis anterior (TA) muscle from mice in (a). Scale bars represent 100 µm. Data are presented as mean ± SEM. (**c**). Immunofluorescence imaging of tdTomato expression in frozen unfixed liver (i.v.), spleen (i.v.), lung (i.v.) tissues, and cryopreserved FFPE-prepared muscle (i.m.) from mice in (a). Sections were counterstained with DAPI or hematoxylin to visualize nuclei. Shown are representative images. (**d**). tdTomato expression was assessed in injected tibialis anterior muscle from Ai14 or WT C57BL/6 mice 5 days after i.m. injection with Cre RNA-LNP using immunohistochemistry (IHC). Shown are representative images with scale bar indicating 100 µm. 5 ROIs (250 µm x 250 µm) thought to be near injection site were selected per muscle, and the percentage of muscle fibers that are tdTomato+ within each ROI's was calculated. Plotted is the mean percentage per biologically independent animal (n = 3 mice, repeated 3 independent times). Data are presented as mean ± SEM. Analyzed by unpaired two-tailed Student's t-test. (**e**). Quantification of tdTomato positive immune cells from the spleen of Ai14 mice injected i.v. or i.m. with 5 µg of Cre RNA-LNP (n = 3 mice, repeated 3 independent times). Data are presented as the proportion of transfected cells within each immune cell subset and shown as mean ± SEM. (**f**). Mean expression of immune cell subsets in the spleen is plotted as a fraction of total tdTomato+ CD45+ cells. (**g**). Quantification of tdTomato+ immune cells (CD45 +) from the ipsilateral popliteal, iliac, or inguinal lymph nodes of Ai14 mice (n = 4, repeated 2 independent times) i.m. injected with irrelevant RNA (Ctrl) or Cre RNA.WT by flow cytometry. Representative flow plots shown. Data are presented as mean ± SEM. ns: not significant, analyzed by unpaired two-tailed Student's t-test.

https://doi.org/10.1038/s41587-026-03099-z

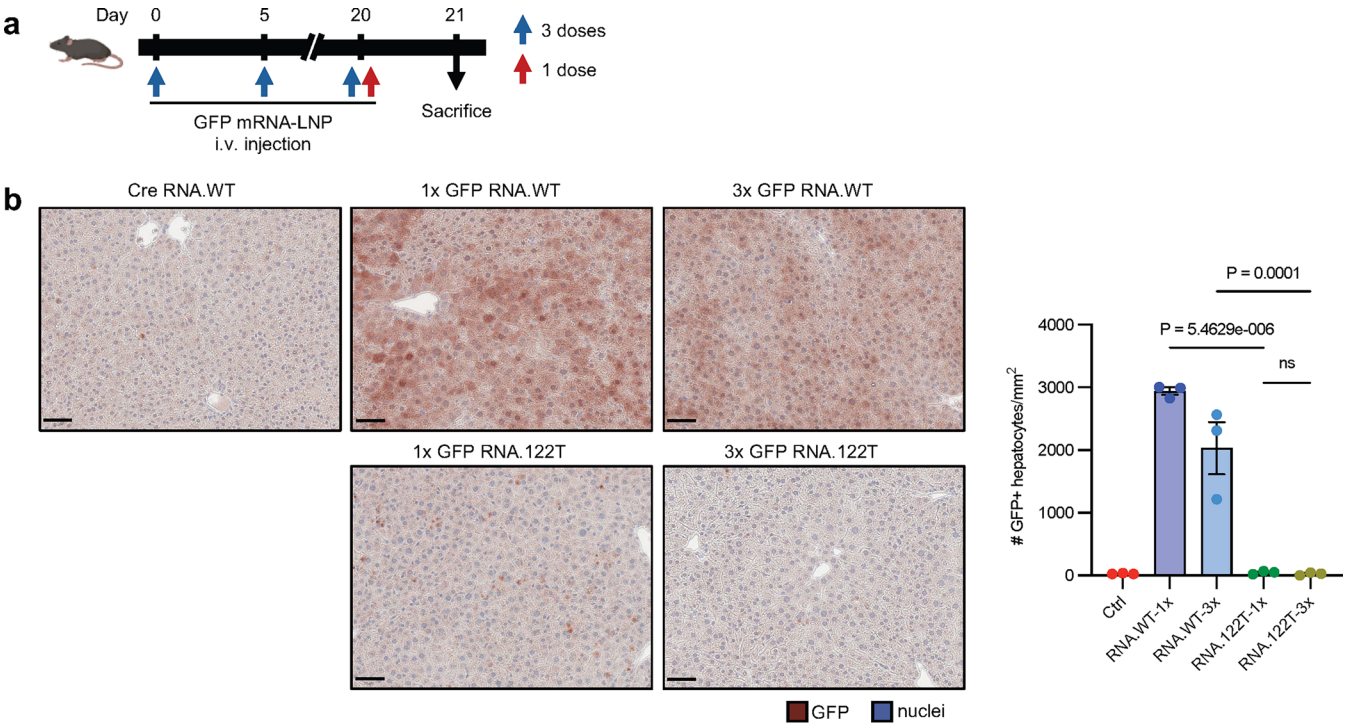

Extended Data Fig. 3 | See next page for caption.

https://doi.org/10.1038/s41587-026-03099-z

Extended Data Fig. 3 | miRNA target sites mediate robust silencing with repeat dosing. (**a**). Schematic of the experiment for (b-c) (created with BioRender.com). (**b**). GFP expression in liver of C57BL/6 mice ($n = 3$) 24 h after i.v. injection of 1 or 3 doses of GFP RNA.WT or RNA.122T-LNP was assessed using IHC. Shown are representative images with scale bar indicating 50 µm. Quantification of number of GFP+ hepatocytes per unit area. Significance assessed using one-way ANOVA with Tukey's multiple comparison test between all experimental groups. (**c**). Quantification of GFP+ immune cells (CD45 +) in spleen by flow cytometry. Significance assessed using one-way ANOVA with Tukey's multiple comparison test between all experimental groups. (**d**). BALB/c mice ($n = 4$) were i.v. injected with 20 µg GFP RNA.WT or RNA.122 T or PBS (Ctrl). Serum was collected 24 hrs after injection and assayed for protein biomarkers by Olink Target 96 Exploratory Panel. Volcano plot showing differential protein abundance between RNA.WT compared to PBS control. The x-axis shows ΔNPX values ($\log_2$ scale), calculated as the difference in normalized protein expression between RNA.WT and PBS groups. Statistical significance was analyzed using a linear model with Benjamini-Hochberg false discovery rate correction. Proteins with FDR < 0.05 are highlighted in red. (**e**). Correlation plot comparing Olink NPX values for each protein analyte measured in mouse serum 24 hr after RNA-LNP injection, as described in (d). Each point represents the mean NPX for one protein. A linear regression line is in blue, and an identity line (y = x) is in dashed black line. Error bars, mean ± SEM. ns: not significant.

https://doi.org/10.1038/s41587-026-03099-z

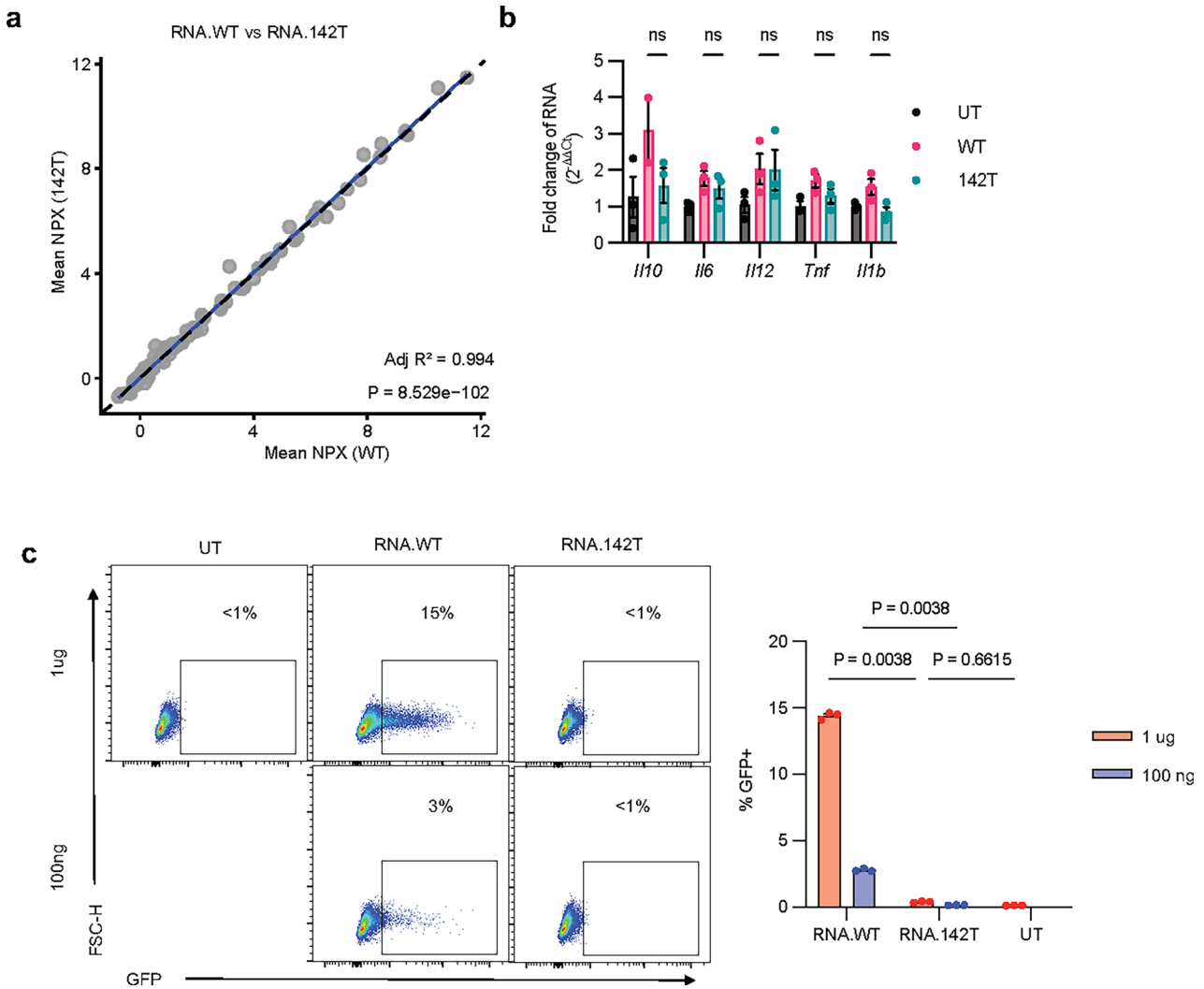

Extended Data Fig. 4 | RNA.142 T expression is silenced in monocytes. (**a**). Bone marrow-derived dendritic cells were treated with 1 ug/ml GFP RNA.WT or RNA.142 T LNP labeled with a DiI+ lipid dye (n = 3 biological replicates). After 24 hrs, culture supernatant was assayed for protein biomarkers by Olink Target 96 Exploratory Panel. Correlation plot comparing Olink NPX values for each protein analyte between RNA.WT and RNA.142T-treated cells shown. Each points represents the mean NPX for one protein. A linear regression line is in blue, and an identity line (y = x) is in dashed black line. (**b**). Relative mRNA expression of *Il6*, *Il12*, *Il10*, *Il1b*, and *Tnf* in DiI+ BMDCs from (a) normalized to untreated (UT) controls. Gene expression was quantified by RT-qPCR and normalized to *Gapdh*. Error bar, mean ± SEM. ns: not significant. Statistical significance was analyzed by one-way ANOVA with Tukey's multiple comparison test.(**c**). GFP expression in primary splenic monocytes 18 h following transfection with 100 ng or 1 µg GFP RNA.WT or RNA.142 T was quantified by flow cytometry (n = 3 biological replicates). UT: un-transfected. Error bars, mean ± SEM. ns: not significant. Significance assessed using one-way ANOVA with Tukey's multiple comparison test between all experimental groups.

https://doi.org/10.1038/s41587-026-03099-z

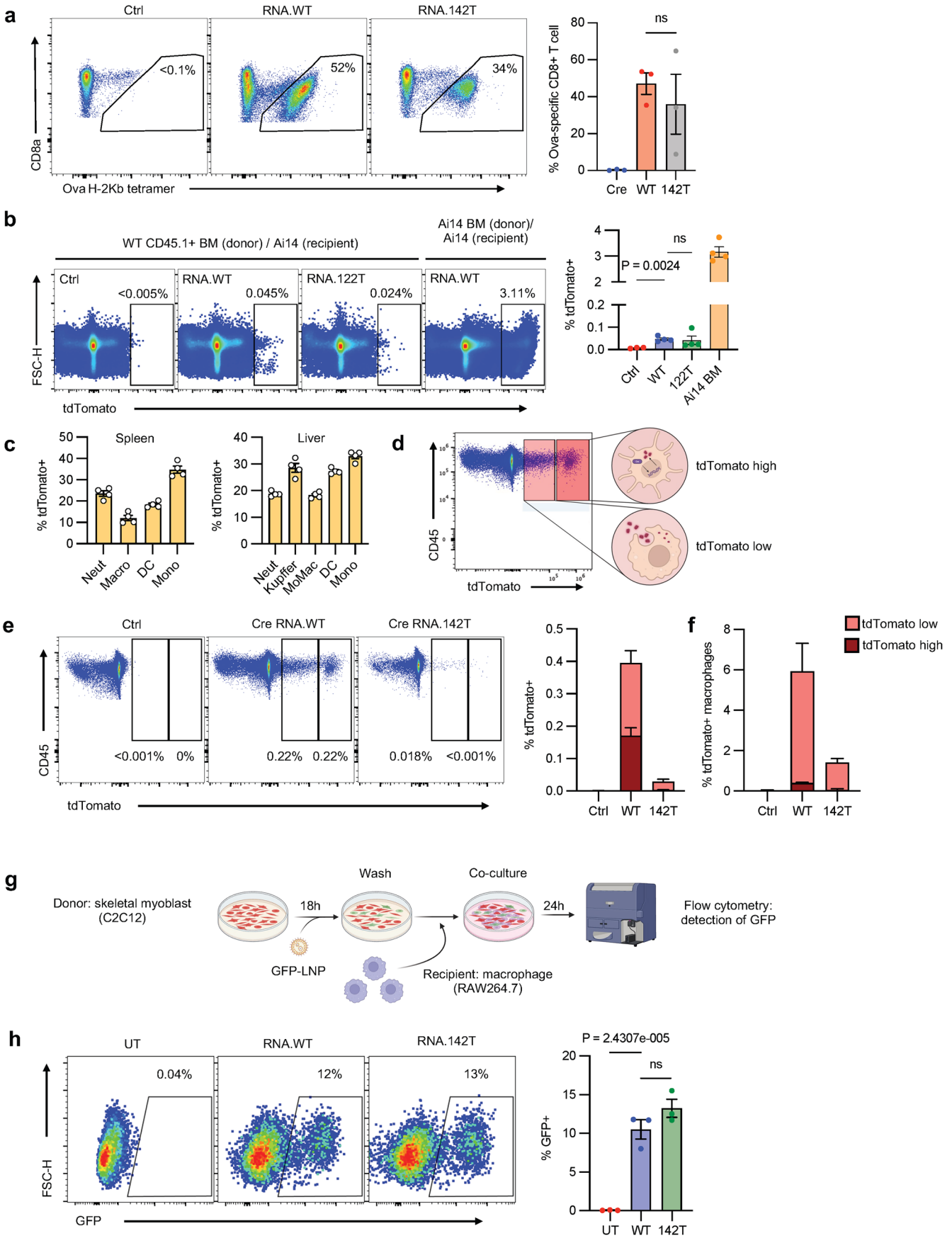

Extended Data Fig. 5 | See next page for caption.

https://doi.org/10.1038/s41587-026-03099-z

Extended Data Fig. 5 | pAPC acquisition of RNA-derived antigen from transfected non-pAPCs surpasses expression from transfection with RNA.142 T. (**a**). C57BL/6 mice (*n* = 3, repeated 3 independent times) were i.v. injected with 20 µg Ova RNA.WT or RNA.142 T or irrelevant RNA (Ctrl) using a prime/boost schedule 21 days apart. Frequency of Ova-specific CD8 + T cells within splenic CD8 + T cells were analyzed by flow cytometry 5 days post-boost using SIINFEKL H-2Kb tetramer. Representative dot plots shown. (**b**). Lethally irradiated CD45.2 + Ai14 mice (*n* = 4) were reconstituted with CD45.1 + WT C57BL/6 bone marrow (BM) before i.v. injection with irrelevant RNA (Ctrl) or Cre RNA.WT or RNA.122 T. As a positive control, recipient Ai14 mice were reconstituted with Ai14 BM prior to Cre RNA.WT injection. tdTomato expression in spleen CD45.1+ cells for WT BM donor groups and CD45.2+ cells for Ai14 BM donor group 3 days post-injection was analyzed by flow cytometry. Representative flow cytometry plots shown. (**c**). Expression of tdTomato in immune cell subsets of the spleen (left) and liver (right) of Ai14 mice reconstituted with Ai14 BM and injected with Cre RNA.WT from (b). tdTomato expression was quantified by flow cytometry. (**d**). Schematic showing flow cytometry analysis for (e) and (f) (created with BioRender.com). Cells from Ai14 mice that have taken up and expressed Cre RNA will undergo Cre-mediated recombination and removal of a *loxP*-flanked STOP cassette upstream of tdTomato. Subsequently, tdTomato will be constitutively expressed under the ROSA26 promoter, leading to high tdTomato expression as detected by flow cytometry, whereas cells that have taken up tdTomato exogenously will have lower tdTomato expression. (**e**). Quantification of tdTomato^{lo} and tdTomato^{hi} immune cells (CD45 +) from the iliac lymph nodes of Ai14 mice (n = 4, repeated 2 independent times) i.m. injected with irrelevant RNA (ctrl), Cre RNA.WT, or Cre RNA.142 T by flow cytometry. Representative flow plots shown. (**f**). Quantification of tdTomato^{lo} and tdTomato^{hi} macrophages (F4/80 + CD11b +) from the iliac lymph nodes of Ai14 mice (n = 4, repeated 2 independent times) i.m. injected with irrelevant RNA (ctrl), Cre RNA.WT, or Cre RNA.142 T by flow cytometry. (**g**). Schematic showing experimental set-up for (h) (created with BioRender.com). C2C12 cells were transfected with GFP RNA.WT or RNA.142T-LNP for 18 h. Following washing to remove LNP from the media, RAW264.7 cells were co-cultured with the C2C12 cells for 24 h. GFP expression was detected by flow cytometry. (**h**). Expression of GFP by RAW264.7 cells (CD45 + F4/80 +) (n = 3 biological replicates). Representative flow cytometry plots shown. UT: un-transfected. Error bar, mean ± SEM. ns: not significant. Statistical significance was analyzed by unpaired two-tailed Student's t-test.

https://doi.org/10.1038/s41587-026-03099-z

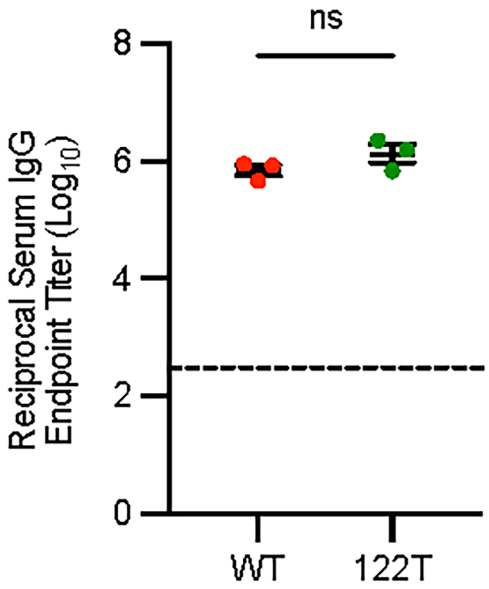

Extended Data Fig. 6 | Assessment of anti-GFP antibody titers induced by hepatocyte-silenced RNA-LNP. BALB/c mice ($n = 3$, repeated 2 independent times) were injected i.v. with 20 µg GFP RNA.WT or RNA.122 T on days 0, 5, and 20. Anti-GFP IgG antibody titers were assessed in sera obtained on day 25 (5 days post-second boost). The limit of detection is indicated by a dotted line. Error bar, mean ± SEM. ns: not significant. Statistical significance was analyzed by unpaired two-tailed Student's t-test.

https://doi.org/10.1038/s41587-026-03099-z

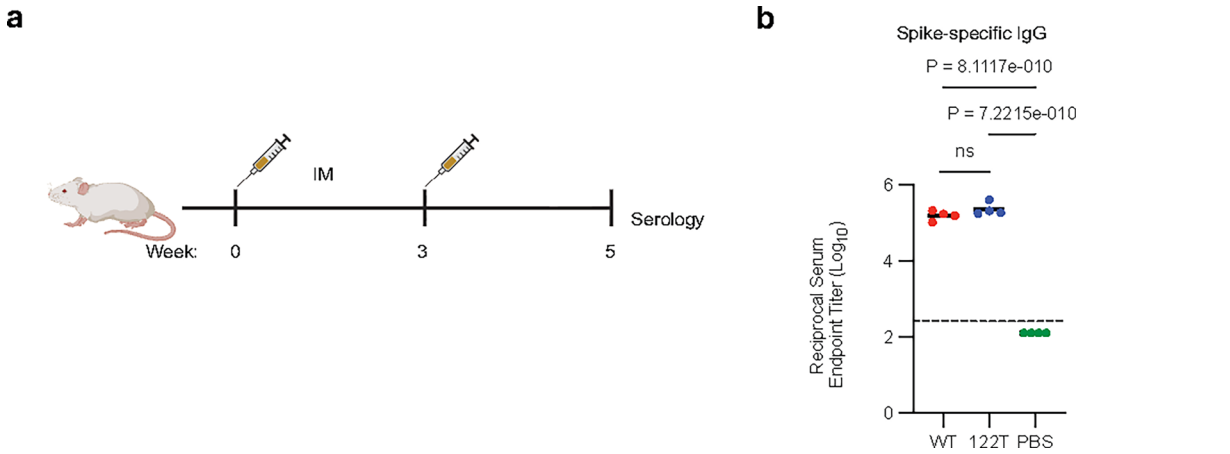

Extended Data Fig. 7 | SARS-CoV-2 Spike RNA.WT and RNA.122 T vaccination elicits comparable antibody and CD4 + T cell responses to mRNA-1273 vaccine. (**a**). BALB/c mice ($n = 4$) were injected i.m. with 1 µg Spike RNA.WT at week 0 and 3. Blood and spleens were obtained at week 5 (2 weeks post-boost) to assess antibody titers (created with BioRender.com). Experimental set-up based off vaccination schedule by DiPiazza et al., Immunity, 2021. (**b**). Serum anti-Spike IgG from mice in (a) was assessed 2 weeks post-boost. The limit of detection is indicated by a dotted line, and values below the limit of detection were assigned a value of half the limit of detection. Error bar, mean ± SEM. ns: not significant. Statistical significance was analyzed by one-way ANOVA followed by Tukey's multiple comparison test between all experimental groups.

https://doi.org/10.1038/s41587-026-03099-z

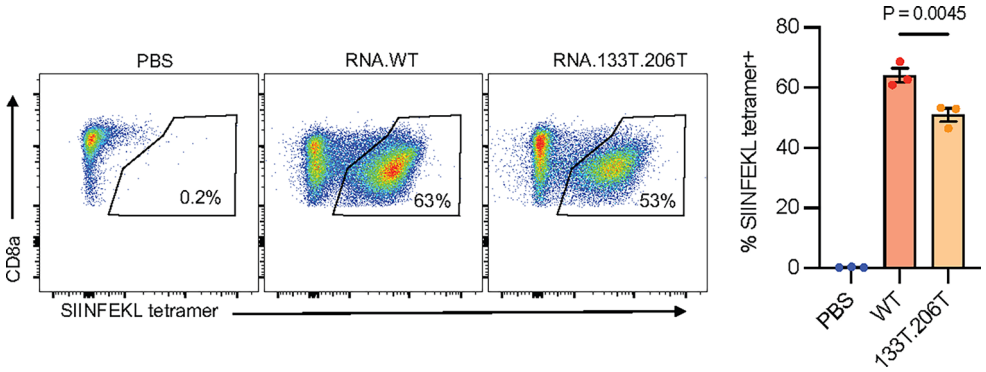

Extended Data Fig. 8 | Assessment of hematopoietic and myocyte influence on antigen-specific CD8 T cell response to intramuscular injected RNA-LNP. C57BL/6 mice ($n = 3$, repeated 2 independent times) were injected i.m. with 5 µg Ova RNA.WT or RNA.133 T.206 T on days 0, 5, and 20. Fraction of SIINFEKL-specific $CD8^+$ T cells within CD8 + T cells in the spleen 5 days post-boost was measured by flow cytometry using SIINFEKL H-2Kb tetramer. Representative flow cytometry plots shown. Error bar, mean ± SEM. ns: not significant. Statistical significance was analyzed by unpaired two-tailed Student's t-test.

nature portfolio

Corresponding author(s): Brian D. Brown

Last updated by author(s): Jan 16, 2026

Reporting Summary

Nature Portfolio wishes to improve the reproducibility of the work that we publish. This form provides structure for consistency and transparency in reporting. For further information on Nature Portfolio policies, see our Editorial Policies and the Editorial Policy Checklist.

Statistics

For all statistical analyses, confirm that the following items are present in the figure legend, table legend, main text, or Methods section.

n/a	Confirmed
☐	☒ The exact sample size (*n*) for each experimental group/condition, given as a discrete number and unit of measurement
☐	☒ A statement on whether measurements were taken from distinct samples or whether the same sample was measured repeatedly
☐	☒ The statistical test(s) used AND whether they are one- or two-sided *Only common tests should be described solely by name; describe more complex techniques in the Methods section.*
☐	☒ A description of all covariates tested
☐	☒ A description of any assumptions or corrections, such as tests of normality and adjustment for multiple comparisons
☐	☒ A full description of the statistical parameters including central tendency (e.g. means) or other basic estimates (e.g. regression coefficient) AND variation (e.g. standard deviation) or associated estimates of uncertainty (e.g. confidence intervals)
☐	☒ For null hypothesis testing, the test statistic (e.g. *F*, *t*, *r*) with confidence intervals, effect sizes, degrees of freedom and *P* value noted *Give P values as exact values whenever suitable.*
☒	☐ For Bayesian analysis, information on the choice of priors and Markov chain Monte Carlo settings
☒	☐ For hierarchical and complex designs, identification of the appropriate level for tests and full reporting of outcomes
☐	☒ Estimates of effect sizes (e.g. Cohen's *d*, Pearson's *r*), indicating how they were calculated

Our web collection on statistics for biologists contains articles on many of the points above.

Software and code

Policy information about availability of computer code

Data collection	No code was used in data collection.
Data analysis	Microsoft Excel (Version 16.78) Prism 10 for macOS (Version 10.6.1) QuPath (Version 0.6.0) ImageJ (Version 2.14.0) FlowJo (Version 10.10.0)

For manuscripts utilizing custom algorithms or software that are central to the research but not yet described in published literature, software must be made available to editors and reviewers. We strongly encourage code deposition in a community repository (e.g. GitHub). See the Nature Portfolio guidelines for submitting code & software for further information.

Data

Policy information about availability of data

All manuscripts must include a data availability statement. This statement should provide the following information, where applicable:

- Accession codes, unique identifiers, or web links for publicly available datasets
- A description of any restrictions on data availability
- For clinical datasets or third party data, please ensure that the statement adheres to our policy

No public datasets were generated or analyzed during the current study. Therefore, no data are available, and no restrictions apply.

Research involving human participants, their data, or biological material

Policy information about studies with human participants or human data. See also policy information about sex, gender (identity/presentation), and sexual orientation and race, ethnicity and racism.

Reporting on sex and gender	N/A
Reporting on race, ethnicity, or other socially relevant groupings	N/A
Population characteristics	N/A
Recruitment	N/A
Ethics oversight	N/A

Note that full information on the approval of the study protocol must also be provided in the manuscript.

Field-specific reporting

Please select the one below that is the best fit for your research. If you are not sure, read the appropriate sections before making your selection.

☒ Life sciences ☐ Behavioural & social sciences ☐ Ecological, evolutionary & environmental sciences

For a reference copy of the document with all sections, see nature.com/documents/nr-reporting-summary-flat.pdf

Life sciences study design

All studies must disclose on these points even when the disclosure is negative.

Sample size	The sample size was determined based on a convenience sampling approach with n = 3-5 mice per group as specified. Statistical power calculations were not performed. Majority of experiments were repeated at least twice with separate cohort of n=3-5 mice.
Data exclusions	No data was excluded from the analyses. All data points were included in the final analysis unless they were affected by technical errors (e.g., failure in data collection or equipment malfunction). The exclusion criteria, if any, were not pre-established, as all mice that were part of the study were considered valid for analysis.
Replication	All attempts at replication were successful, and the experimental conditions were replicated to ensure reproducibility. No specific findings failed to replicate, but variability between individual mice should be considered.
Randomization	Mice were randomly assigned to experimental groups to reduce potential bias in treatment allocation. Randomization was achieved using a random number generator to select which mice were assigned to each experimental group. The allocation was done prior to beginning any experimental procedures.
Blinding	Blinding was applied during the imaging analyses for counting measurements. The individuals performing the imaging analysis and counting of outcomes (e.g., cell counts, lesion quantification, etc.) were blinded to the experimental group allocation. This was done to minimize any potential observer bias in the analysis of images. However, blinding was not possible for the treatment assignment because the researchers were aware of which treatment the mice received. Despite this, blinding in the subsequent image analysis steps ensured that the outcome data collection was objective and unbiased.

Reporting for specific materials, systems and methods

We require information from authors about some types of materials, experimental systems and methods used in many studies. Here, indicate whether each material, system or method listed is relevant to your study. If you are not sure if a list item applies to your research, read the appropriate section before selecting a response.

Materials & experimental systems

n/a	Involved in the study
☐	☒ Antibodies
☐	☒ Eukaryotic cell lines
☒	☐ Palaeontology and archaeology
☐	☒ Animals and other organisms
☒	☐ Clinical data
☒	☐ Dual use research of concern
☒	☐ Plants

Methods

n/a	Involved in the study
☒	☐ ChIP-seq
☐	☒ Flow cytometry
☒	☐ MRI-based neuroimaging

Antibodies

Antibodies used

Flow cytometry (1:200 dilution or per manufacturer's sheets)
CD11b FITC (Biolegend, M1/70, 101206)
CD11b APC (Biolegend, M1/70, 101212)
FR-b APC (Biolegend, 10/FR2, 153305)
XCR1 APC-Cy7 (Biolegend, ZET, 148224)
XCR1 APC (Biolegend, ZET, 148206)
I-A/I-E BV510 (Biolegend, M5/114.15.2, 107636)
F4/80 BV605 (Biolegend, BM8, 123133)
CD11c BV650 (Biolegend, N418, 117339)
CD64 BV711 (Biolegend, X54-5/7.1, 139311)
CD64 PE (Biolegend, X54-5/7.1, 139304)
CD45 BV510 (Biolegend, 30-F11, 103138)
CD45 BV785 (Biolegend, 30-F11, 103149)
CD45 Spark NIR 685 (Biolegend, 30-F11, 103168)
CD3 Spark UV 387 (Biolegend, 17A2, 100284)
CD4 PE (Biolegend, RM4-5, 100512)
CD4 BV605 (Biolegend, RM4-5, 100548)
CD4 BV785 (Biolegend, RM4-5, 100552)
CD25 PE/Dazzle594 (Biolegend, PC61, 102048)
CD44 BV510 (Biolegend, IM7, 103044)
CD62L BV570 (Biolegend, MEL-14, 104433)
TIM3 BV711 (Biolegend, RMT3-23, 119727)
CD8a BV785 (Biolegend, 53-6.7, 100750)
CD69 APC-Cy7 (Biolegend, H1.2F3, 104526)
IFNγ PE-Cy7 (Biolegend, XMG1.2, 505826)
Granzyme B APC (Biolegend, QA16A02, 372204)
Granzyme B Pacific Blue (Biolegend, GB11, 515408)
NKp46 PerCP-eFluor710 (eBioscience, 29A1.4, 46-3351-82)
CD45.1 PE-Cy7 (eBioscience, A20, 25-0453-82)
Ly-6G Alexa Fluor 700 (eBioscience, 1A8-Ly6g, 56-9668-82)
Ly-6C eFluor 450 (eBioscience, HK1.4, 48-5932-82)
PD-1 PerCP-eFluor 710 (eBioscience, J43, 46-9985-82)
CD3e FITC (eBioscience, 145-2C11, 11-0031-82)
NK1.1 APC-eFluor 780 (eBioscience, PK136, 47-5941-82)
CD19 eFluor 450 (eBioscience, eBio1D3 (1D3), 48-0193-82)
CD64 PE-Cy7 (eBioscience, 10.1, 25-0649-42)
Foxp3 PE-Cy7 (eBioscience, FJK-16s, 25-5773-82)
B220 BUV563 (BD Biosciences, RA3-6B2, BDB748868)
CD8a APC (BD Biosciences, 53-6.7, BDB561093)
Siglec-F APC-Cy7 (BD Biosciences, E50-2440, BDB565527)
CD25 PE (BD Biosciences, PC61, BDB565527)

Tetramer (1:100 dilution)
anti-HYLSTQSAL H2-Kd tetramer APC (NIH Tetramer Core Facility)
anti-SIINFEKL H2-Kb tetramer APC (NIH Tetramer Core Facility)
anti-VNFNFNGL H2-Kb tetramer APC (NIH Tetramer Core Facility)

IHC/CyCIF
GFP (Takara, JL-8, 632381,1:200)
DsRed (Takara, 632496, 1:500)
F4/80 (Cell Signaling, D2S9R, 70076S, 1:200)
CD31 (Abcam, EPR17259, ab182981, 1:1000)
CD8a (Cell Signaling, D4W2Z, 98941S, 1:200)
B220 (eBioscience, RA3-6B2, 14-0452-82, 1:200)
Ly-6G (Biolegend, 1A8, 127601, 1:200)

aSMA (Abcam, ab5694, 1:200)
MHC I (Cell Signaling, E8E7N, 76828, 1:200)
Cleaved Caspase 3 (Cell Signaling, 9661, 1:400)

Validation

These antibodies have been verified by the supplier. All antibodies used are from commercial sources and validation data are available on the manufacturer's website based on their catalogue numbers.

Eukaryotic cell lines

Policy information about cell lines and Sex and Gender in Research

Cell line source(s)	HEK293T, Phoenix-Eco, RAW264.7, MEL, AML12, 3T3, BCL-1, C2C12, and Huh7 were obtained from ATCC. GFP-A20 is a murine lymphoma cell line on the BALB/c background (H-2Kd) and expressing enhanced green fluorescent protein (GFP) and generated previously.
Authentication	Authentication provided by ATCC.
Mycoplasma contamination	All cell lines used tested negative for mycoplasma contamination.
Commonly misidentified lines (See ICLAC register)	N/A

Animals and other research organisms

Policy information about studies involving animals; ARRIVE guidelines recommended for reporting animal research, and Sex and Gender in Research

Laboratory animals	C57BL/6, BALB/c, Ai14, and B6.SJL-Ptprca Pepcb/BoyJ (B6 CD45.1) mice were obtained from the Jackson Laboratory (JAX# 000664, 000651, 007914, 028062, respectively) and housed in the Mount Sinai vivarium during use. Jedi mice on a BALB/c background, derived from B10.D2 Jedi mice generated in the Brown lab via backcrossing.
Wild animals	N/A
Reporting on sex	Female animals were used throughout all experiments. Animals were age-matched (6-12 weeks old).
Field-collected samples	N/A
Ethics oversight	All mice were housed at the Icahn School of Medicine at Mount Sinai under the approval of the Institutional Animal Care and Usage Committee (IACUC) protocol (IACUC-2018-0070) and complied with local, state and federal regulations.

Note that full information on the approval of the study protocol must also be provided in the manuscript.

Plants

Seed stocks	N/A
Novel plant genotypes	N/A
Authentication	N/A

Flow Cytometry

Plots

Confirm that:

☒ The axis labels state the marker and fluorochrome used (e.g. CD4-FITC).

☒ The axis scales are clearly visible. Include numbers along axes only for bottom left plot of group (a 'group' is an analysis of identical markers).

☒ All plots are contour plots with outliers or pseudocolor plots.

☒ A numerical value for number of cells or percentage (with statistics) is provided.

Methodology

Sample preparation	Peripheral blood was collected from the orbital sinus. A20 lymphoma tumors, spleens and lymph nodes were collected in RPMI with 2% FBS on ice, homogenized by smashing using the plunger of a 3 mL syringe (BD Biosciences), and filtered through a 70-µm cell strainer. Erythrocytes for peripheral blood, spleens, and tumors were removed using 1x RBC lysis buffer (Thermo, 00-4333-57). Bone marrow cells were flushed from femur and tibia bones, homogenized, and filtered through 70 µm cell strainer, before erythrocytes were removed by hypotonic lysis. For tissue preparation of livers, transcardiac perfusion with 10mL ice-cold PBS was first performed. Livers were collected in RPMI with 2% FBS on ice, minced using a sterile blade, and digested with 1 mg/mL collagenase IV (Gibco #17104019), 40 µg/mL DNase I (Signma-Aldrich, DN25) dissolved in PBS with 5% FBS for 30 min at 37°C with constant shaking. Liver homogenate was filtered through a 70 µm cell strainer. Cells were resuspended in 40% Percoll (Cytiva), previously adjusted with 10X PBS, and layered onto 70% Percoll. Percoll gradient was centrifuged at 400g for 25 min at 24°C with no acceleration and no brake. The layer containing immune cells were collected and washed with FACS buffer (PBS with 2% FBS and 0.5mM EDTA).
Instrument	Immune cells were analyzed using a LSRFortessa X-20 (BD Biosciences) or Aurora 5L (Cytek).
Software	BD FACSDiva™ Software Cytek Spectroflo FlowJo 10.10.0
Cell population abundance	Cell sorting was not employed in this study.
Gating strategy	In vitro cell lines: The gating strategy for cell lines began with FSC-A vs. SSC-A gating to exclude debris, followed by doublet discrimination using FSC-A vs. FSC-H. A live/dead stain was applied to exclude non-viable cells. After gating on viable single cells, fluorescence was analyzed to identify transduced or transfected cells. GFP-expressing cells were identified using the FITC channel, while tdTomato-expressing cells were detected using the PE channel. Fluorescence-minus-one (FMO) controls were used to define thresholds for positive and negative populations. Liver: The gating strategy for liver cells began with FSC-A vs. SSC-A gating to exclude debris, followed by doublet discrimination using FSC-A vs. FSC-H, followed by SSC-A vs SSC-H. A live/dead stain was applied to exclude non-viable cells, and CD45+ leukocytes were selected. For bone marrow chimeras reconstituted with CD45.1 hematopoietic cells, CD45.1+ cells were then selected. For lymphoid cells, T cells (CD3+), B cells (B220+ CD3-), and NK cells (CD3- B220- NKp46+) were identified. For myeloid cells (CD3- B220- NKp46-), neutrophils (Ly6G+)w ere first gated. Among Ly6G- cells, monocyte-derived macrophages (F4/80+, CD64+, FOLR2-), Kupffer cells (F4/80+ CD64+ FOLR2+), monocytes (CD11b+ Ly6C+), and dendritic cells (CD11c+ MHCII+) were gated. Fluorescence-minus-one (FMO) controls were used to define positive and negative populations for all markers. Spleen/LN: The gating strategy for spleen/LN cells began with FSC-A vs. SSC-A gating to exclude debris, followed by doublet discrimination using FSC-A vs. FSC-H, followed by SSC-A vs SSC-H. A live/dead stain was applied to exclude non-viable cells, and CD45+ leukocytes were selected. For lymphoid cells, T cells (CD3+), B cells (B220+ CD3-), and NK cells (CD3- B220- NKp46 +) were identified. For myeloid cells (CD3- B220- NKp46-), neutrophils (Ly6G+) were first gated. Among Ly6G- cells, monocyte-derived macrophages (F4/80+, CD64+, FOLR2-), eosinophils (Siglec-F+), monocytes (CD11b+ Ly6C+), and dendritic cells (CD11c+ MHCII+) were gated. Fluorescence-minus-one (FMO) controls were used to define positive and negative populations for all markers. For T cell (CD45+ CD3+) phenotyping, CD4+ and CD8+ T cells were gated. Antigen-specific T cells were identified as tetramer+, and adoptively transferred T cells were identified as CD45.1+.

☒ Tick this box to confirm that a figure exemplifying the gating strategy is provided in the Supplementary Information.